INVESTIGATIONS OF RARE EARTH MANGANITES AND METAL NANOPARTICLES

A THESIS SUBMITTED IN PARTIAL FULFILMENT OF THE REQUIREMENTS OF THE DEGREE OF MASTER OF SCIENCE AS A PART OF THE INTEGRATED Ph.D PROGRAMME

BY

R. SRINIVASA GOPALAN

TO

MANIPAL ACADEMY OF HIGHER EDUCATION

THROUGH

JAWAHARLAL NEHRU CENTRE FOR ADVANCED SCIENTIFIC RESEARCH BANGALORE

FEBRUARY 1997

STATEMENT

Certified that work reported here has been done under my supervision at Jawaharlal Nehru Centre for Advanced Scientific Research, Bangalore.

Professor C. N. R. Rao, F.R.S

ACKNOWLEDGEMENTS

I'm thankful to Prof. C. N. R. Rao for suggesting the problems, providing me the facilities and for his constant and invaluable guidance and I hope that I'll continue to receive the same in the years to come.

I thank Dr. G. U. Kulkarni his guidance, support, day to day assitance and encouragement throughout.

I thank my faculty advisor, Prof. J. Chandrasekhar, Dr. W. H. Madhusudan,(coordinator), Prof. V. Krishnan,(Head Academics), Prof. S. Chandrasekharan (Int. PhD coordinator,IISc) and Prof. S. Ramsesha (Chairman, SSCU) and many other faculties of JNCASR and Chemical Sciences Division(IISc) for their guidance and help at various stages.

I thank my collaborators Dr. Mahesh and Mr S. Ayyappan for their efforts. I thank my labmates and friends for their help and encouragement.

I am greatly indebted to my family members for all the affection and support they have given me.

PREFACE

This thesis comprises of two parts, the first deals with investigations on Charge Ordering phenomenon and the second with the synthesis and characterisation of metal nanoparticles.

In the first part we discuss the electric and magnetic properties of the rare earth manganites with perovskite structure [$Gd_{0.45}Sr_{0.55}MnO_3$, $Gd_{0.5}Ca_{0.5}MnO_3$, $Pr_{0.5}Ca_{0.5-x}Ba_xMnO_3$ (x = 0, 0.125, 0.25)]. The effect of varying average ionic radius of the A-site on the electric and magnetic properties have been investigated. The samples were characterised using X-ray, DC magnetic susceptibility and electrical resistivity measurements and the local structure around the Mn ion have been studied using EXAFS.

In the second part methods of prepartion and characterisation of stabilised metal nanoparticles of Ag, Au and Cu have been discussed. They were prepared by reducing the respective metal salts a) from their solutions using ethanol as the reducing agent and Polyvinyl pyrrolidone as the stabiliser and b) reducing the metal salt intercalated montmorillonite using polyol. The metal particles so formed were characterised using X-ray diffraction (XRD), UV-absorption spectroscopy and Transmission electron microscopy (TEM). From the line width broadening of XRD and from TEM photographs the average particle sizes were determined.

Contents

PART I

CHARGE ORDERING IN RARE EARTH MANGANITES

Introduction

Rare earth manganites ($LnMnO_3$) crystallize in a perovskite structure [1] formed by the corner sharing octahedra of oxygen ions with Mn^{3+} and Ln^{3+} in the six- and twelve-coordinated sites respectively, as shown in Fig.1. The Mn^{3+} ion (d^4) in the octahedral environment with each of the low lying triply degenerate t_{2g} orbitals and one of the e_g orbitals half filled is Jahn-Teller active and undergoes tetragonal distortion giving rise to four short Mn O distances in the ab plane and two long Mn-O along the c axis. As the concentration of Mn^{3+} ion in these manganites is quite high (one per unit cell), the distortions about the adjacent Jahn-Teller ions are cooperative and therefore dictate the lattice structure as a whole [2]. Accordingly, the crystal structure of stoichiometric $LaMnO_3$ is orthorhombic [3] (a = 5.443, b = 5.594 and c = 7.805 Å) with two pairs of short distances (1.91 and 1.96 Å) in the ab plane and two long distances (2.19 Å) along the c-axis.

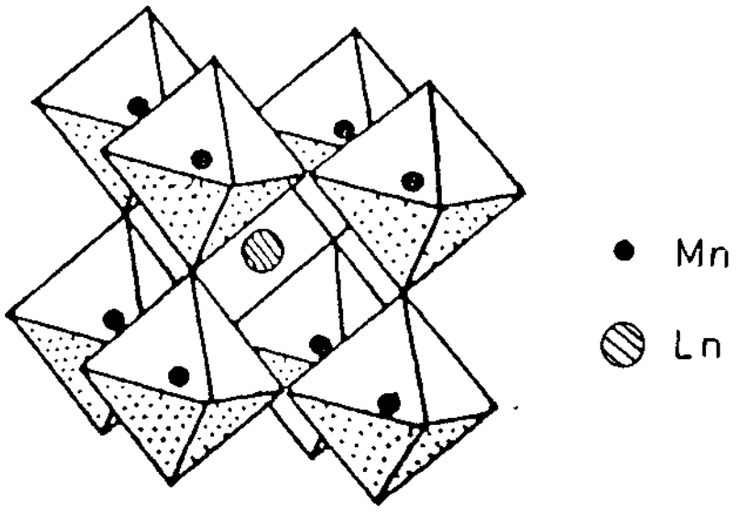

Fig.1. Perovskite structure of $LnMnO_3$ (from ref.1b).

The extent of distortion from the ideal cubic perovskite structure, ABO_3 is generally measured in terms of a tolerance factor, t. which is defined as

$$t = (r_A + r_O)/ \sqrt{2}(r_B + r_O)$$

where r_A, r_B and r_O are the radii of the A, B, and O ions respectively. For cubic perovskites, t is close to 1. Rare earth manganites with the t values ~ 0.9 adopt perovskite structures in non-cubic lattices. The cell remains orthorhombic up to Ln = Gd and is hexagonal for the higher members.

As can be seen from Fig.2, the neighboring Mn^{3+} interact via oxygen. The e_g orbital of Mn^{3+} is hybridized with the oxygen 2p orbitals along the Mn-O-Mn bond direction and the resulting super exchange interaction according to the Anderson-Goodenough-Kanamori rules [4], leads to antiferromagnetic ordering. Electron hopping is highly restricted in this situation and therefore $LnMnO_3$ are generally insulating and antiferromagnetic.

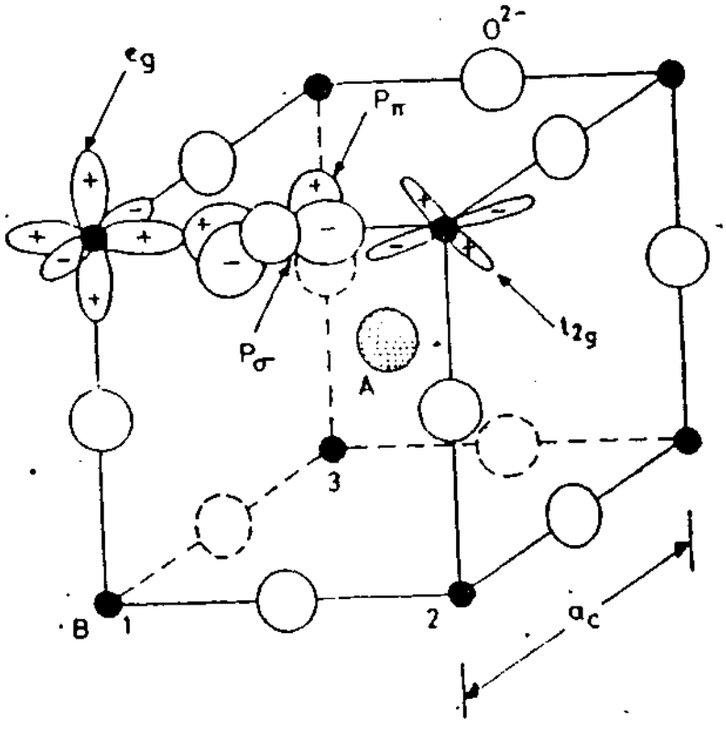

Fig.2. The perovskite structure showing the 180° cation - anion - cation (Mn-O-Mn) interaction. The angle corresponding to Mn-O-Mn interaction depends on the crystal structure. There is no direct Mn-Mn interaction in these perovskites (from ref. 1c).

The radius of the Ln^{3+} plays an important role. The Mn-O-Mn bond is nearly linear for bigger cations like La^{3+} (152°) and on decreasing the radius of the Ln^{3+} ion, the angle decreases due to the buckling of the MnO_6 octahedra. The degree of orbital overlap also decreases making the e_g states more localized. The conductivity and the magnetic ordering temperature therefore decrease with smaller rare earth cations. For illustration, $LaMnO_3$ is insulating and undergoes antiferromagnetic ordering around 140 K [3], while $PrMnO_3$ and $GdMnO_3$ [5] are more insulating with lower antiferromagnetic ordering temperatures (80 and 21 K respectively).

•

Introducing Mn^{4+} in the perovskite structure, by creating defects in the Ln or Mn sites or by aliovalent doping in the Ln site by divalent cations like Ca, Sr, Ba and Pb bring about interesting changes in the electric and magnetic properties [6-8] specially noteworthy being the recent discovery of giant magnetoresistance (GMR) in these materials [9-11]. The defect structure, $La_{1-x}\ Mn_{1-x}\ O_3$, is found to become a ferromagnetic metal (T_C ~ 210 K) for x = 0.04 with the Mn^{4+} concentration of about 25 %. A maximum of 33% Mn^{4+} may be introduced with x = 0.055 and this composition as well shows ferromagnetic and metallic behavior below 210 K

(see Fig.3) [6,7]. Unlike the defect structures, aliovalent doping can in general be performed over the entire composition range. In $La_{1-x}Ca_xMnO_3$ for example [8], both the end members $LaMnO_3$ and $CaMnO_3$ are antiferromagnetic and insulating. The oxide becomes ferromagnetic in a limited composition range (x = 0.1-0.5) and concomitantly exhibits metal-like conductivity below T_C. The Curie temperature increases from ~ 160 K for x = 0.1 to around 250 K for x = 0.3 and decreases to ~200 K on increasing x further before the material becomes antiferromagnetic above x = 0.5. The above is understood on the basis of double-exchange mechanism of Zener [12] which involves an electron hopping from Mn^{3+} (d^4, $t_{2g}^3e_g^1$, S = 2) to Mn^{4+} (d^3 t_{2g}^3, S = 3/2) via the oxide ion so that Mn^{3+} and Mn^{4+} ions exchange places

$$Mn^{3+}\,O^{2-}\,Mn^{4+} \rightarrow Mn^{4+}\,O^{2-}\,Mn^{3+}$$

This involves the transfer of an electron from Mn^{3+} site to the central oxide ion and simultaneously the transfer of an electron from the oxide ion to the Mn^{4+} site. The integral defining the exchange energy is non vanishing in such a system only if the spins of the two d shells are parallel. That is, the

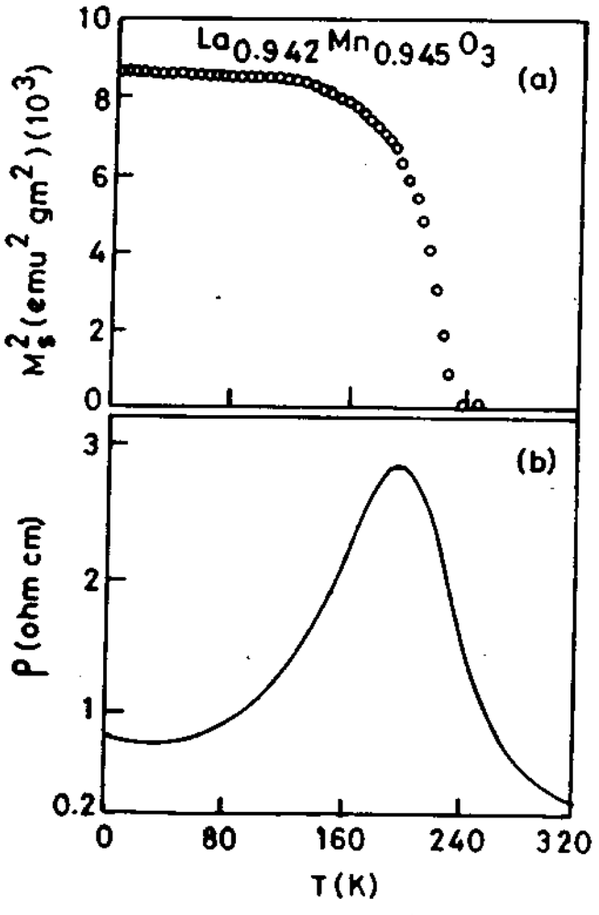

Fig.3. Variation of a) the magnetisation and b) resistivity of $La_{0.945}Mn_{0.945}MnO_3$ with temperature (from ref. 7).

lowest energy of the system is the one with a parallel alignment of spins on the Mn^{3+} and Mn^{4+} ions. This is indeed a novel situation where the lining up of the spins of the incomplete d orbitals of the adjacent Mn ions is accompanied by an increase in the rate of hopping of electrons and therefore an increase in the electrical conductivity. Thus the mechanism that leads to enhanced electrical conductivity requires a ferromagnetic coupling. However, when the population of Mn^{4+} is significant, an additional Mn^{4+}-O-Mn^{4+} antiferromagnetic interaction sets in and promotes insulating behavior in the material.

In $Ln_{1-x}A_xMnO_3$, the average size of the A-site cation (r_A) has a marked effect on the electronic structure in that it determines the Mn-O-Mn bond angle and the nature of e_g electron [13,14]. Those compositions with smaller r_A`s have localized e_g electrons and with Mn^{4+} population comparable to Mn^{3+} they present an ideal situation for real space ordering of Mn^{3+} and Mn^{4+}. Obviously, such a 'charge ordered' state is insulating and generally antiferromagnetic. Interestingly, the charge ordered state can be melted into a metallic spin-ordered (ferromagnetic) state by the application of a magnetic field giving rise to GMR. For example, applying a magnetic

field of 12T at the charge ordering temperature (158 K) in the case of $Pr_{0.5}Sr_{0.5}MnO_3$ is found to stabilize a ferromagnetic metallic state with a large negative GMR [15]. This fascinating spin and charge ordering phenomena in the rare earth manganites can be described in terms of a generalized phase diagram [14] in Fig.4. The diagram shows that when $<r_A>$ is large (e.g., $La_{1-x}Sr_xMnO_3$), ferromagnetism and associated I-M transition is found, but charge ordering is not observed. With decreasing $<r_A>$, we observe a ferromagnetic state, which transforms to the antiferromagnetic charge-ordered state on cooling (e.g., $Nd_{0.5}Sr_{0.5}MnO_3$). When $<r_A>$ is very small as in $Pr_{0.7}Ca_{0.3}MnO_3$ and $Nd_{0.5}Ca_{0.5}MnO_3$, no ferromagnetism occurs, but there is a charge-ordered state; the ferromagnetic metallic state is created only by the application of a magnetic field to the charge-ordered state. We compare the magnetic and electronic phase diagrams of $Pr_{1-x}Sr_xMnO_3$ and $Pr_{1-x}Ca_xMnO_3$ [16] in Fig.5 to illustrate the effect of the e_g band width.

Investigating local structure around manganese ions in these perovskites is one of the current interests. A recent study [17] of $Nd_{0.5}Ca_{0.5}MnO_3$ has shown a first-order transition at around 200 K with a large change in volume due to charge ordering accompanied by changes in

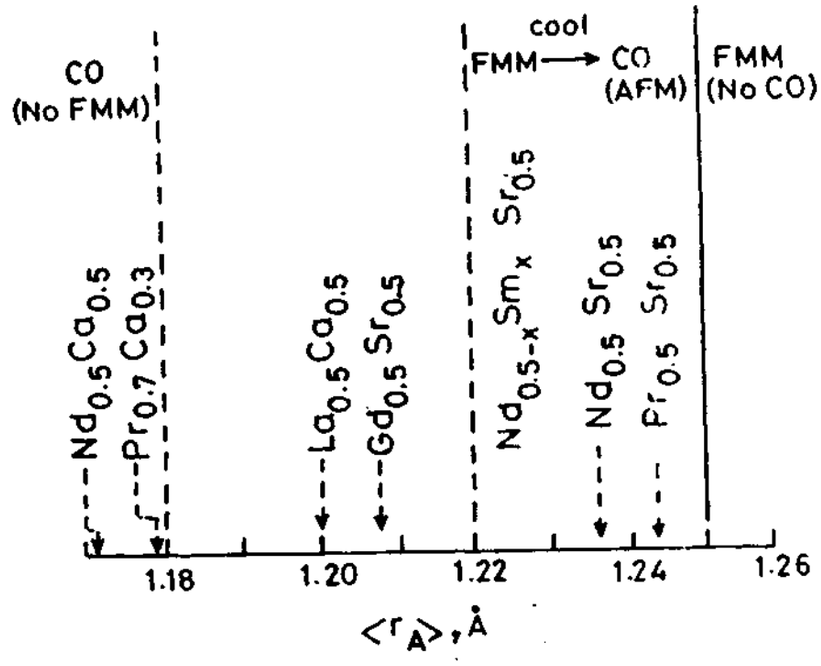

Fig.4. Schematic phase diagram showing the prevalence of charge ordered (CO) and ferromagnetic (FMM) states in $Ln_{1-x}A_xMnO_3$ depending on the average radius of the A - site cation, $< r_A >$ (AFM, antiferromagnetic) (from ref. 14.)

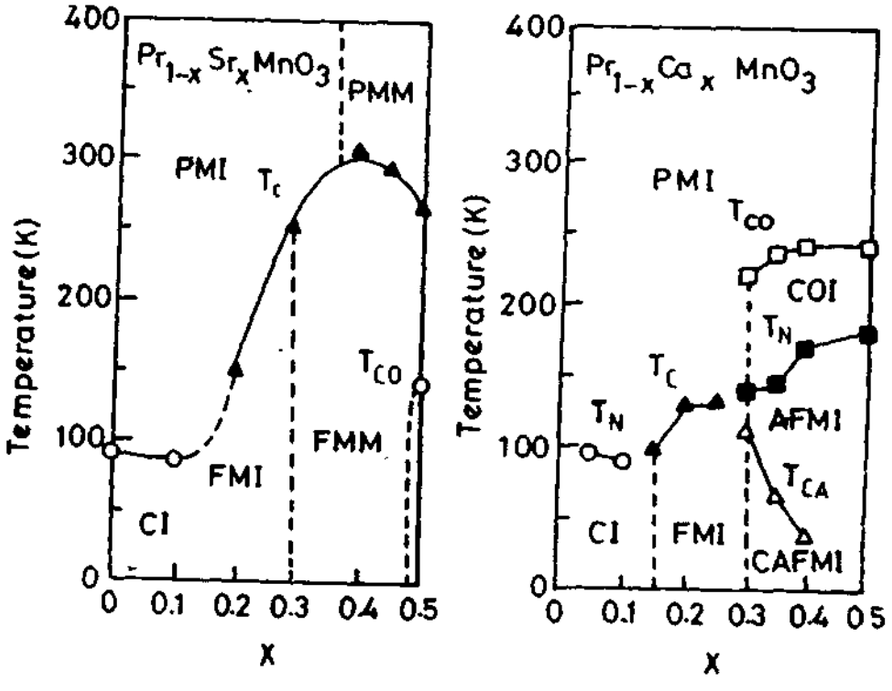

Fig.5. The magnetic and electronic phase diagrams of $Pr_{1-x}Sr_xMnO_3$ and $Pr_{1-x}Ca_xMnO_3$ (adapted from ref. 16). PMI, paramagnetic insulator ; PMM, paramagnetic metal ;CI, canted spin insulator ; FMM, ferromagnetic insulator ; AFMI, antiferromagnetic insulator ; COI, charge ordered insulator ; CAFMI, canted antiferromagnetic insulator.

the bond angles and bond lengths in the ab plane. Tyson et al. [18] have examined local lattice distortions in $La_{0.67}Ca_{0.33}MnO_3$ using EXAFS. They have found two Mn-O bonds at ~2.5 Å and four short bonds at ~1.98 Å in the ferromagnetic metallic state at 80 K. In view of the above discussion, we considered it worthwhile examining the change in the local structure around $Mn^{3+(4+)}$ due to charge ordering and have therefore synthesized and characterized $Gd_{0.5}Ca_{0.5}MnO_3$ and $Gd_{0.45}Sr_{0.55}MnO_3$ whose $\langle r_A \rangle$`s (1.14 and 1.22 Å respectively) fall in two different regimes (I and III) of the phase diagram (see fig). Our purpose was to study the effect of $\langle r_A \rangle$ on charge ordering as well as on the local environment around $Mn^{3+(4+)}$ and we have therefore carried out EXAFS measurements on these compounds at 300 and at 100 K. Our study have indeed revealed important structural changes occurring following charge ordering. We have also studied the effect of Ba substitution in the Ca site (increasing the $\langle r_A \rangle$) in $Pr_{0.5}Ca_{0.5}MnO_3$ on its structure and properties.

Experimental

All the samples were prepared by the standard ceramic method. $Gd_{0.45}Sr_{0.55}MnO_3$ was prepared by mixing stoichiometric amounts of Gd_2O_3, $SrCO_3$ and $MnCO_3$ and preheated at 1273 K in air for 12 hr. The reacted powder was ground, pressed into pellets and reheated at 1473 K in air for 24 hr and then at 1673 K in air for 12 hr. This was followed by heating the sample in oxygen at 923 K for 24 hr.

$Gd_{0.5}Ca_{0.5}MnO_3$ was prepared by mixing stoichiometric amounts of Gd_2O_3, $CaCO_3$, and $MnCO_3$ and preheating it for 12 hr at 1473 K in air. It was then reground, pressed into pellets and reheated at 1673 K for 24 hr.This was followed by heating the compound in oxygen 923 K for 24 hr.

$Pr_{0.5}Ca_{0.5-x}Ba_xMnO_3$ (x = 0, 0.125 and 0.25) were prepared by mixing stoichiometric amounts of Pr_6O_{11}, $CaCO_3$, $BaCO_3$ and $MnCO_3$ and preheating it in air at 1273 K. It was then pelletized, reheated at 1473 K in air for 24 hr and then at 1673 K in air for 12 hr. After this the samples were heated in oxygen at 923 K for 24 h.

Characterization and measurement

The phase purity and the lattice constants of various manganites were determined from powder x-ray diffraction patterns recorded at room temperature on a JEOL JDX-8P diffractometer employing Ni-filtered Cu Kα radiation. Unit cell parameters were derived by least square refinement of the powder diffraction data using PROSZKI program and the parameters are listed in Table 1.

The Mn^{4+} contents in the manganites were determined by redox titrations [19]. The samples were dissolved in a known excess of standardized Ferrous Sulfate solution. The excess Fe^{2+} was then titrated with standardized Potassium Permanganate solution. The number of milliequivalents of iron oxidized by Mn^{3+} and Mn^{4+} was obtained by the difference between the total number of milliequivalents of Fe^{2+} added and the milliequivalents of excess iron determined by titration. A blank titration was been carried out (without the sample) with a known volume of Ferrous Sulfate solution and standardized Potassium Permanganate solution.

Electrical resistivity was measured in the temperature range 20 - 300 K using a four probe technique and the electrical contacts were made using

Table 1

Cell parameters and Mn^{4+} content of the manganites

Compound	Crystal System	Cell parameters (A)	Mn^{4+} (%)
$Gd_{0.5}Ca_{0.5}MnO_3$	Orthorhombic	a = 5.337 b = 5.459 c = 7.497	43
$Gd_{0.45}Sr_{0.55}MnO_3$	Orthorhombic	a= 5.411 b= 5.525 c= 7.641	41
$Pr_{0.5}Ca_{0.5}MnO_3$	Orthorhombic	a = 5.412 b = 5.446 c = 7.651	38
$Pr_{0.5}Ca_{0.375}Ba_{0.125}MnO_3$	Orthorhombic	a = 5.425 b = 5.415 c = 7.669	45
$Pr_{0.5}Ca_{0.25}Ba_{0.25}MnO_3$	Orthorhombic	a = 5.444 b = 5.415 c = 7.705	45

silver paste. DC susceptibility measurements were made in the temperature range 20 - 300 K using a lewis coils force magnetometer. Magnetic fields up to 1000 Oe were used during the measurements. Specific heat capacities of the samples were measured using a Perkin-Elmer DSC-2 differential scanning calorimeter instrument using sapphire as the standard. The specific heat capacities of the samples were determined at an interval of 5 K.

The Mn K-edge absorption spectra of the Gd-manganites were recorded employing a Rigaku spectrometer attached to a rotating anode x-ray generator (RU-200B. Rigaku, Japan) operating at 13 kV, 150 mA. A Ge(220) crystal was used as the monochromator with 0.2 mm slit. Samples equivalent of 18 mg of Mn were pressed into self supporting wafers after mixing with about 100 mg of polyethylene powder. The wafers were 20 mm in diameter and about 0.5 mm thick. An indigenously built cold finger type vacuum cell having Be windows for x-ray transmission was employed for measurements at 100 K and also at room temperature.

Data collection was carried out in the steps of 10 eV in the pre-edge region (6400 - 6530 eV) and 1 eV in the EXAFS region, up to 7100 eV, with

a dwell time of 20 seconds for each data point. Normalized EXAFS,χ was obtained after the pre-edge and the background subtraction.

$$\chi = (\mu-\mu_0)/\mu_0$$

where μ is the absorption coefficient of the sample and μ_0 is that of the free atom computed using spline fitting. The value of E_0 was fixed at the onset of the edge at ~ 6560 eV while calculating the photoelectron wavevector, k

$$k = (2\Pi/h)[2m(E-E_0)]^{1/2}$$

Fourier transforms (FT) were obtained from the normalized EXAFS in the 3.5 - 11 A^{-1} region after weighting the data by k^3. Fourier filtering was then applied to the region of interest (Mn-O peaks) and the curve fitting was carried out using the single scattering plane wave approximation given below

$$\chi = \Sigma_j (N_j/kR_j^2) F_j(k) \exp(-2\sigma_j^2k^2) \exp(-2R_j/\lambda(k)) \sin[2kR_j + \phi_j(k)]$$

where N_j is the number of atoms in the jth coordination shell, k is the photoelectron wave vector, R_j is the distance from the absorber to the jth shell, σ_j represents the root-mean-square deviation of the interatomic distances over R_j (Debye-Waller factor), $\lambda(k)$ is the mean free path of the photoelectron and $\phi_j(k)$ is the total phase-shift due to the jth coordination shell consisting of twice the phase-shift due to the absorber atom, $2\delta_a$ (once

while going out and again while coming back) as well as that due to the back scatterer,$\delta_b(k)$. We have employed McKale's theoretical phase and amplitude parameters[20] in the curve fitting of the fourier filtered data. The procedure was first applied to the EXAFS data of MnO (NaCl structure). We have also used related compounds-$CaMnO_3$ and $GdMnO_3$-as other references.

Results and discussion

We shall first discuss our results on the characterization of Ca and Sr substituted Gd manganites. The x-ray diffraction patterns of $Gd_{0.5}Ca_{0.5}MnO_3$ and $Gd_{0.45}Sr_{0.55}MnO_3$ are shown in Fig.6a,b. All the reflections could be indexed with an orthorhombic cell belonging to Pbnm space group and the cell parameters are given in Table 1. The Mn^{4+} contents obtained from titration are 43 and 41% for the Ca and Sr substituted systems respectively (Table 1).

Both the compositions were found to be insulating down to 90 K as shown in Fig.7. In the magnetic measurements, the slope of the susceptibility

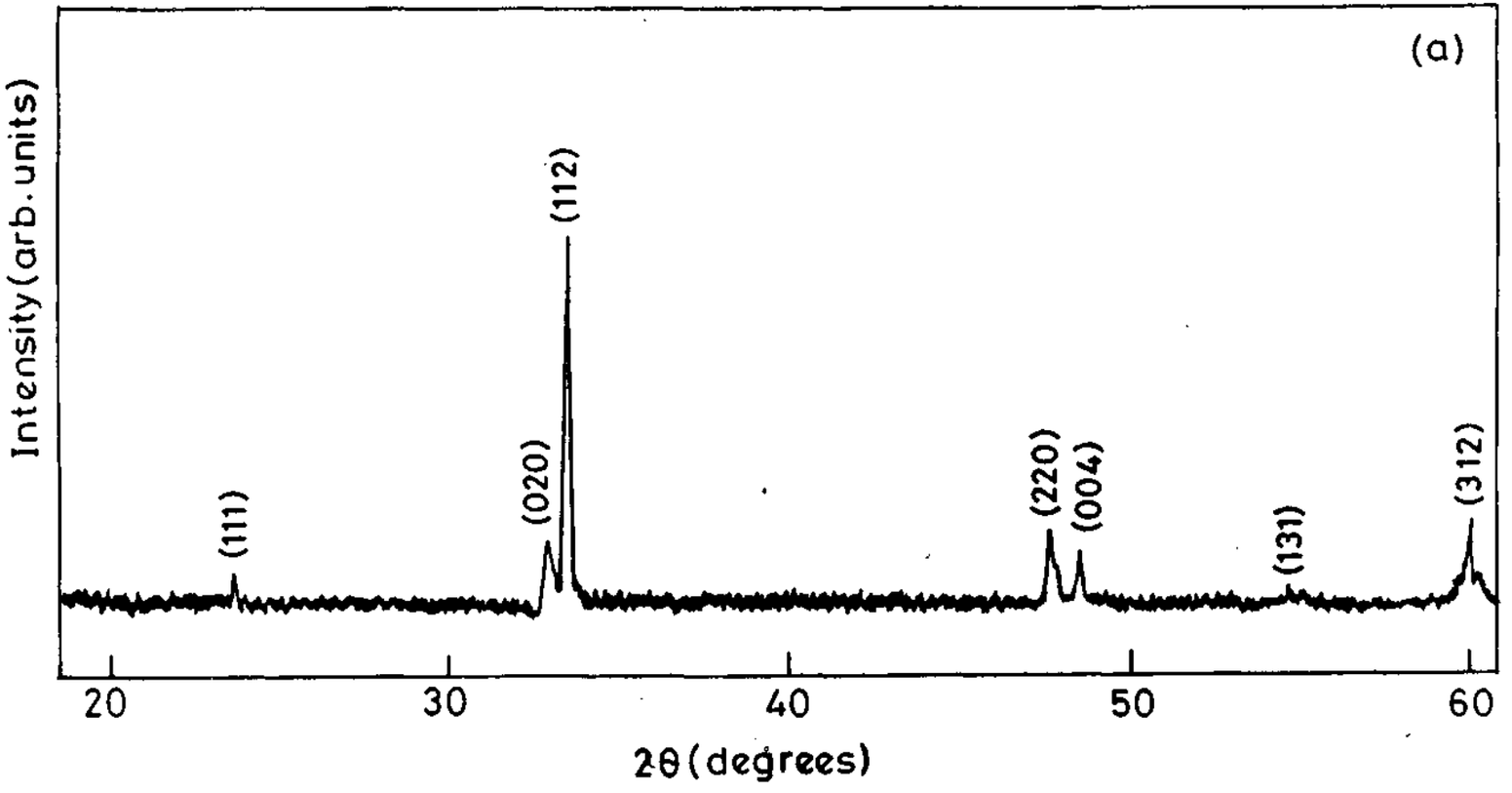

Fig.6. ■ X-ray diffraction patterns of $Gd_{0.5}Ca_{0.5}MnO_3$

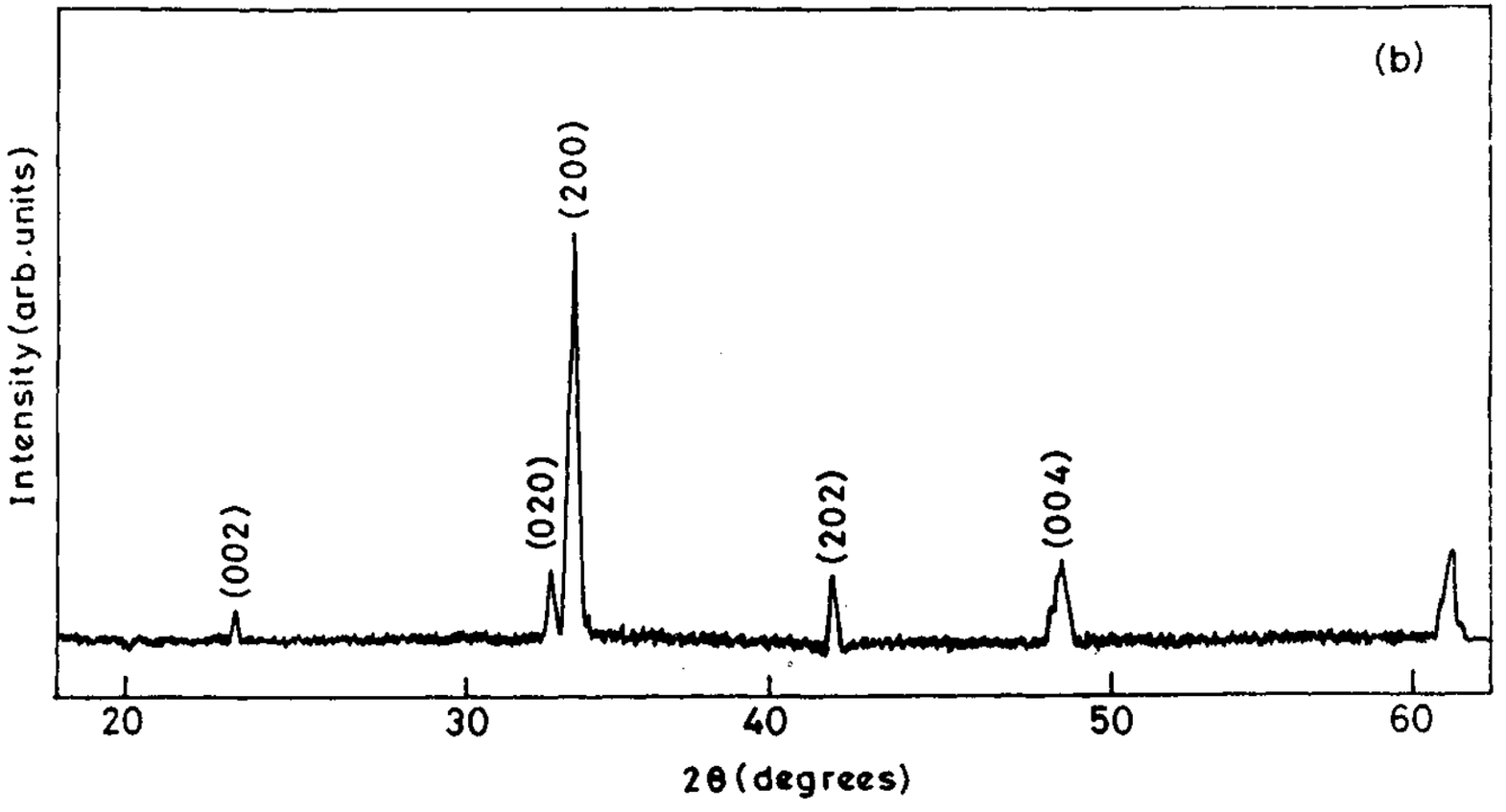

Fig.6b. X-ray diffraction pattern of $Gd_{0.45}Sr_{0.55}MnO_3$.

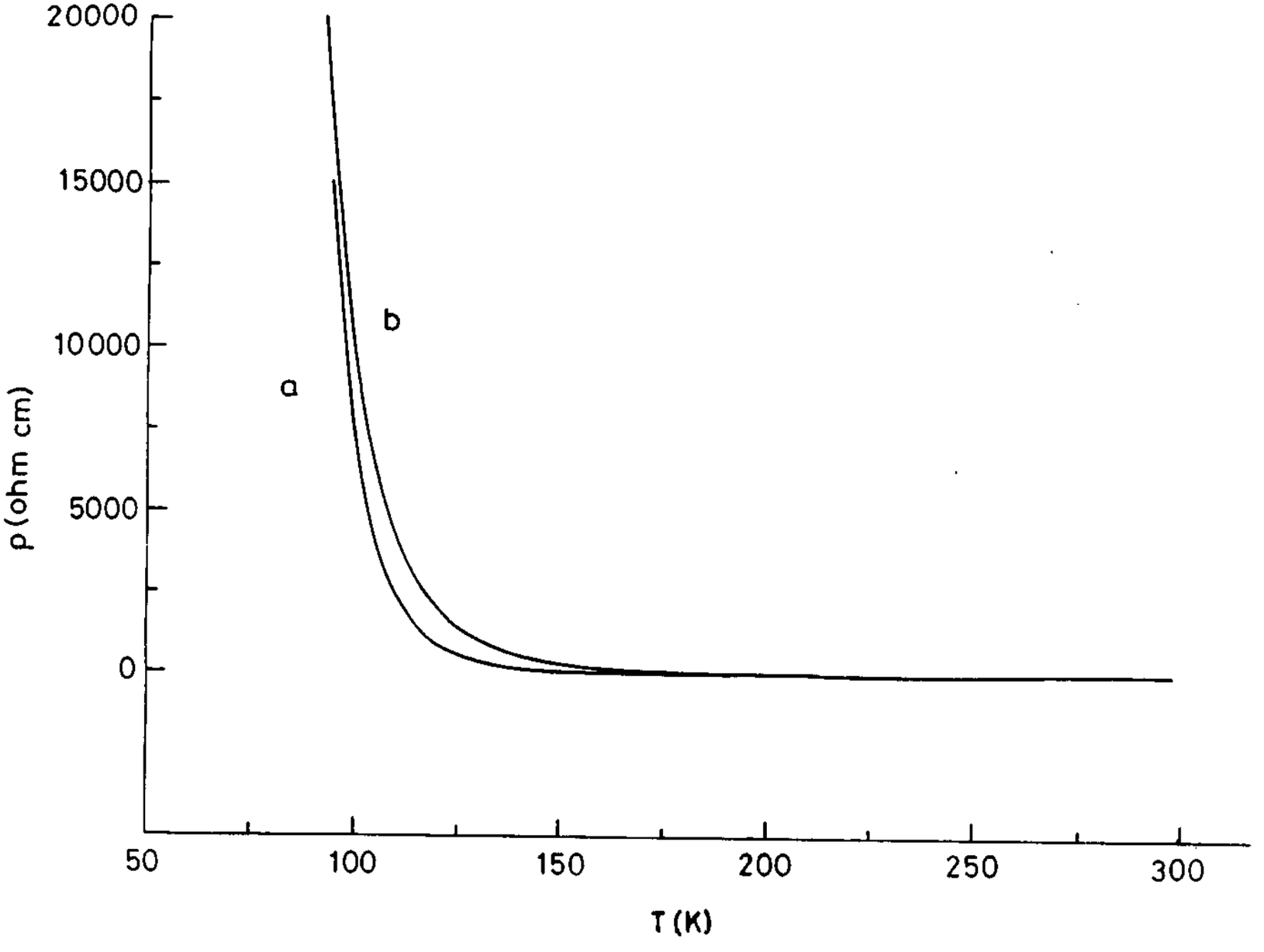

Fig. 7. Temperature variation of resistivity of a) $Gd_{0.5}Ca_{0.5}MnO_3$ and b) $Gd_{0.45}Sr_{0.55}MnO_3$.

curves at low temperature implied negative Curie temperatures arising from antiferromagnetic interactions (Fig.8) in these manganites. The heat capacity data of $Gd_{0.5}Ca_{0.5}MnO_3$ shown in Fig.9 exhibits a well defined feature around 250 K and a broad feature around 170 K and while that of $Gd_{0.45}Sr_{0.55}MnO_3$ has a single feature around 130 K. The electrical resistivity data was obtained as plots of logρ vs. 1/T and $d\log\rho/dT^{-1}$ vs. T to check sensitive variations in the activation energies corresponding to the variations in the heat capacity data. We find that the logρ plot changes slope around 250K for $Gd_{0.5}Ca_{0.5}MnO_3$ and at 120 K for $Gd_{0.45}Sr_{0.55}MnO_3$(Fig.10) and the $d\log\rho/dT^{-1}$ vs. T plots support these observations(Fig.11). We recall that the magnetic susceptibility (see Fig.8) of $Gd_{0.5}Ca_{0.5}MnO_3$ shows two features around 250 and 170K. It appears that the material is in a canted anti-ferromagnetic state at room temperature and changes to paramagnetic state below 250 K before it settles in an antiferromagnetic state around 170 K. The proportion of Mn^{4+} being close to 50% in this compound (Table 1), we consider the transition around 250 K observed in the heat capacity, resistivity and magnetic susceptibility data as due to the charge ordering phenomenon and the transition at 170 K due to the change from a paramagnetic to an antiferromagnetic state. $Gd_{0.45}Sr_{0.55}MnO_3$ on the other hand shows a gradual

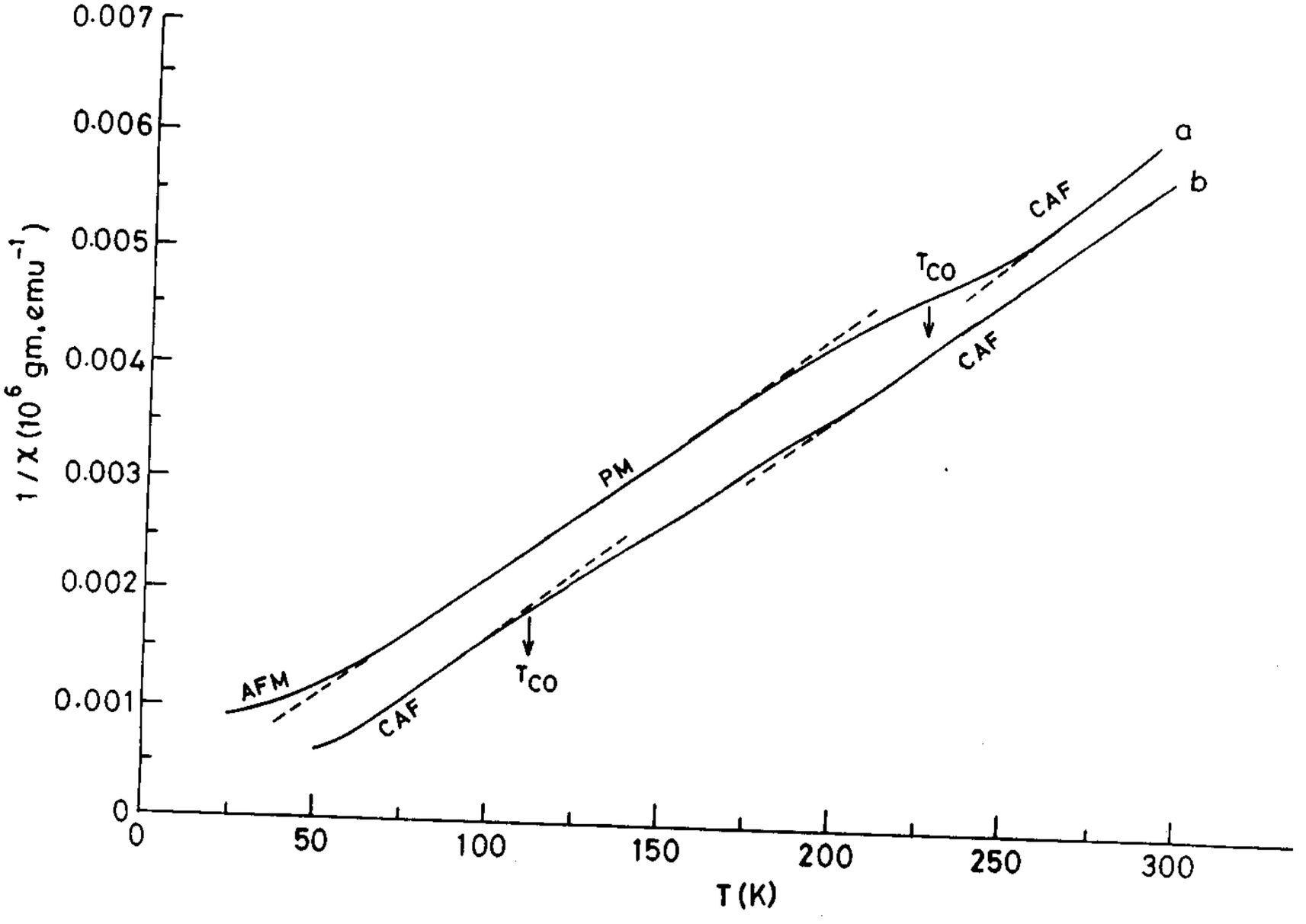

Fig.8. Variation of inverse susceptibility of a) $Gd_{0.5}Ca_{0.5}MnO_3$ and b) $Gd_{0.45}Sr_{0.55}MnO_3$ with temperature.

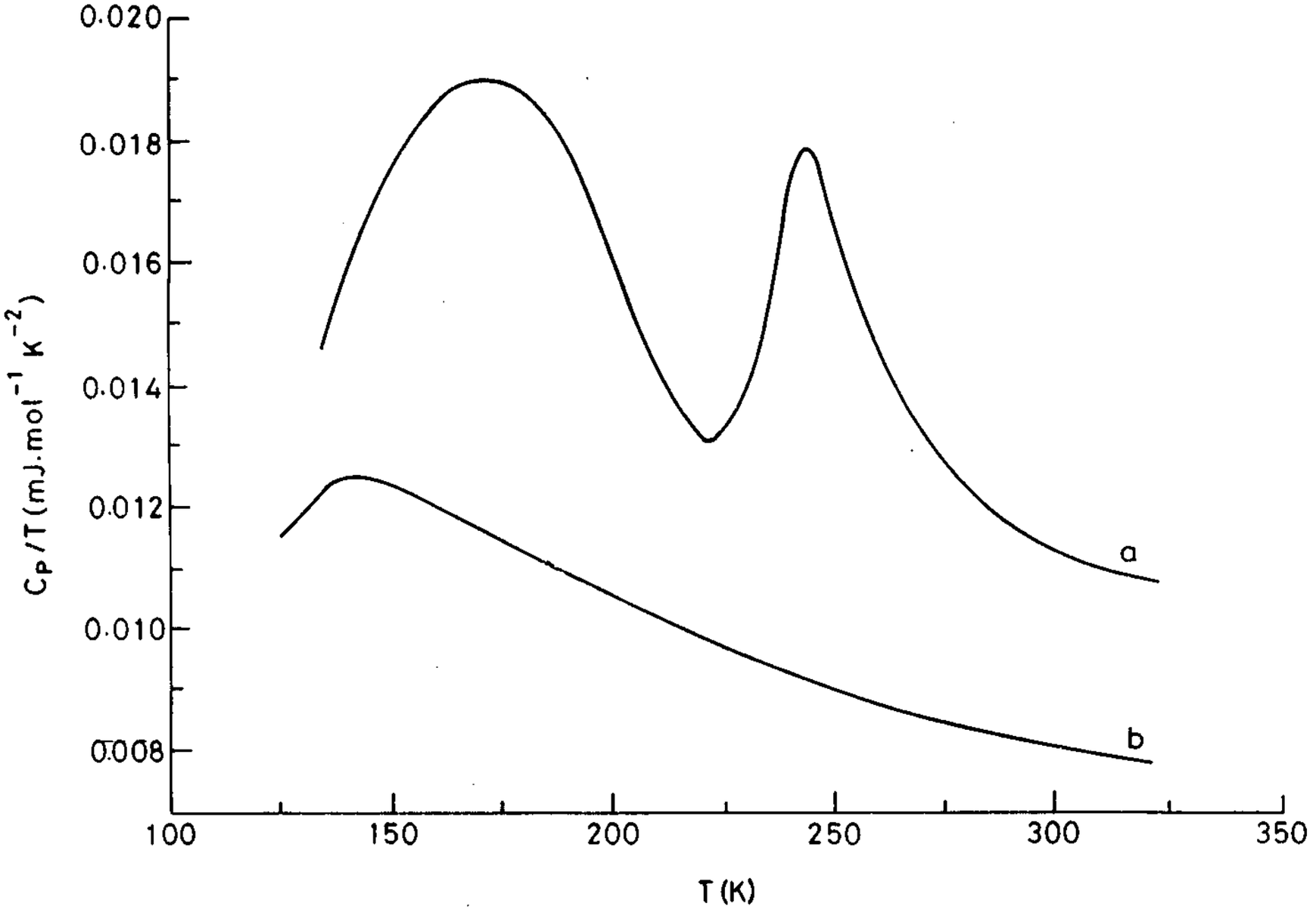

Fig.9. Temperature variation of C_p / T a) $Gd_{0.5}Ca_{0.5}MnO_3$ and b) $Gd_{0.45}Sr_{0.55}MnO_3$ with temperature.

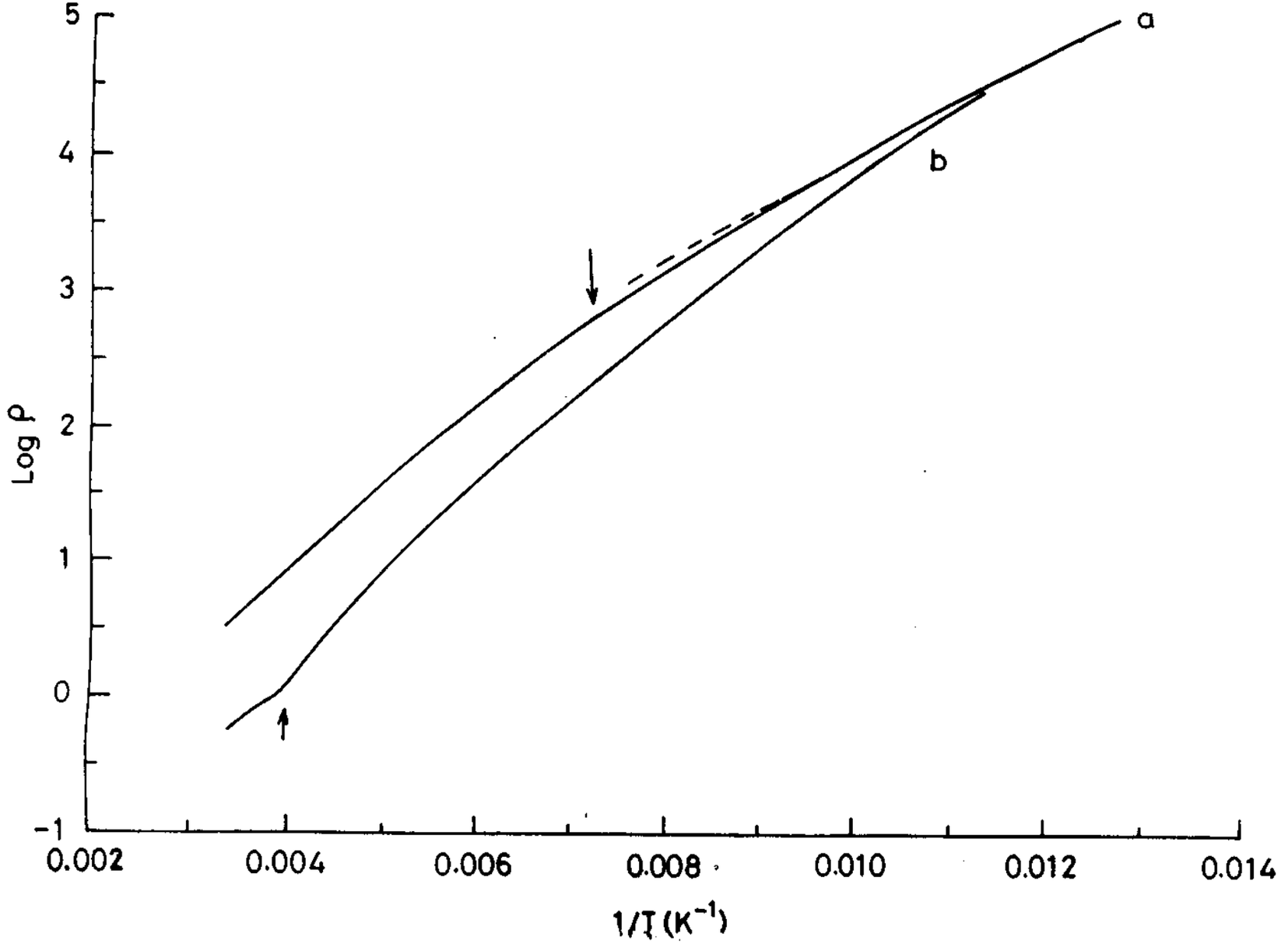

Fig. 10. Variation of log (resistivity) a) $Gd_{0.5}Ca_{0.5}MnO_3$ and b) $Gd_{0.45}Sr_{0.55}MnO_3$ with T^{-1}.

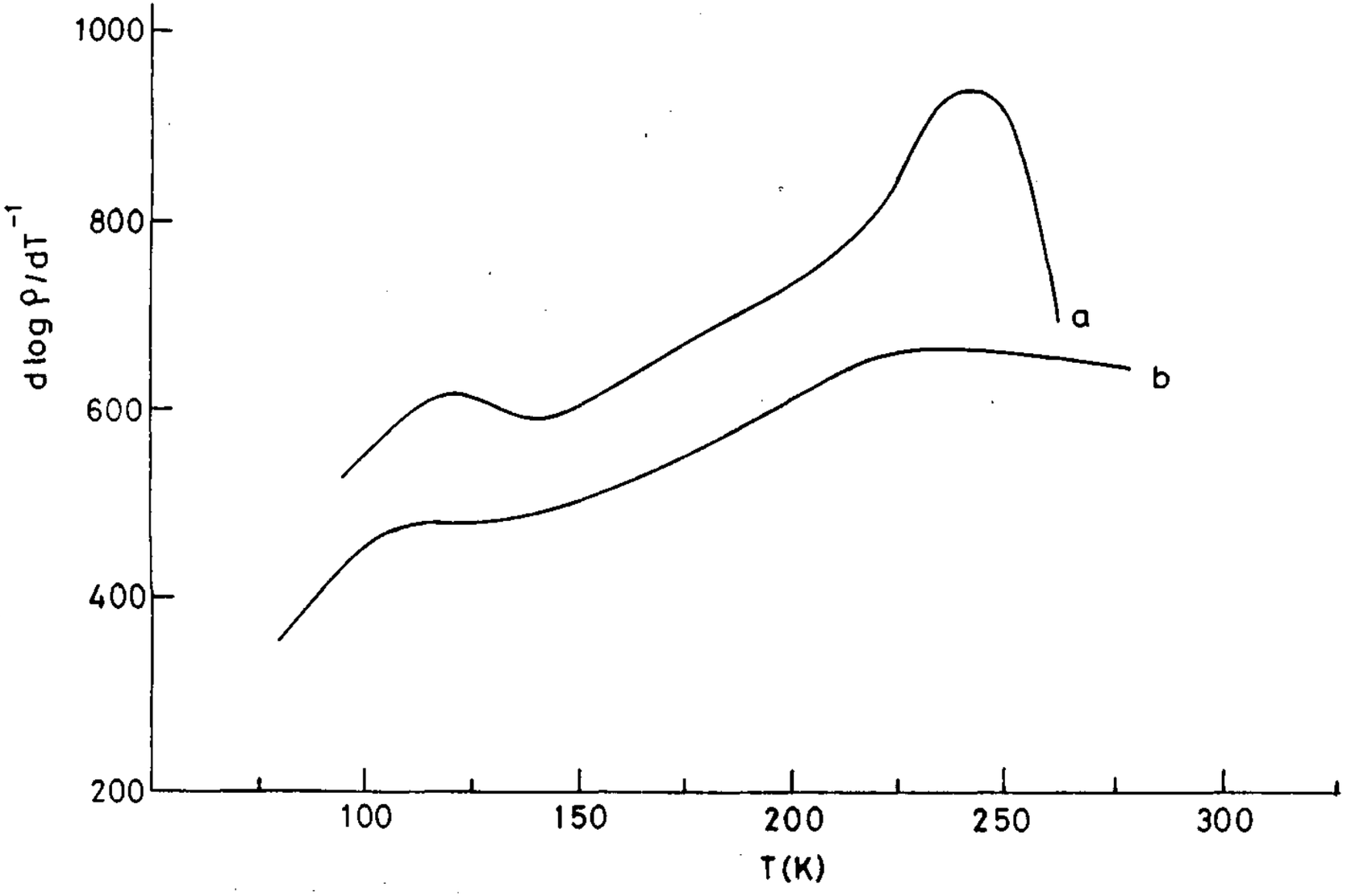

Fig.11. Variation of dlog (resistivity) / dT^{-1} a) $Gd_{0.5}Ca_{0.5}MnO_3$ and b) $Gd_{0.45}Sr_{0.55}MnO_3$ with temperature.

change in its canted antiferromagnetic behavior down to 130 K and finally becomes antiferromagnetic at around 50 K. We also observe changes in the ESR line width around this temperature, which we have shown in Fig.12. We assign the peak observed around 130K in these measurements to, the change in magnetic behavior. We believe that no charge ordering occurs in this composition upto the 50K.

EXAFS results

To begin with, details on the analysis of the EXAFS data of the reference compounds-MnO, $CaMnO_3$ and $GdMnO_3$ are presented. In Fig.13(a), we show the raw EXAFS data of MnO at 300 K. We observe undulations in μ over a range of 600 eV from the Mn edge (~ 6560 eV) which is evident from the normalized EXAFS plot in Fig.13(b). The FT of MnO at room temperature shown in Fig.13c exhibits the first and the second peaks at 1.71 and 2.75 Å corresponding to Mn-O and Mn-Mn coordinations respectively. Curve fitting analysis of the first peak using theoretical Mn-O phase and amplitude parameters gave the Mn-O distance of 2.22 Å with a coordination number of six close to that known from the

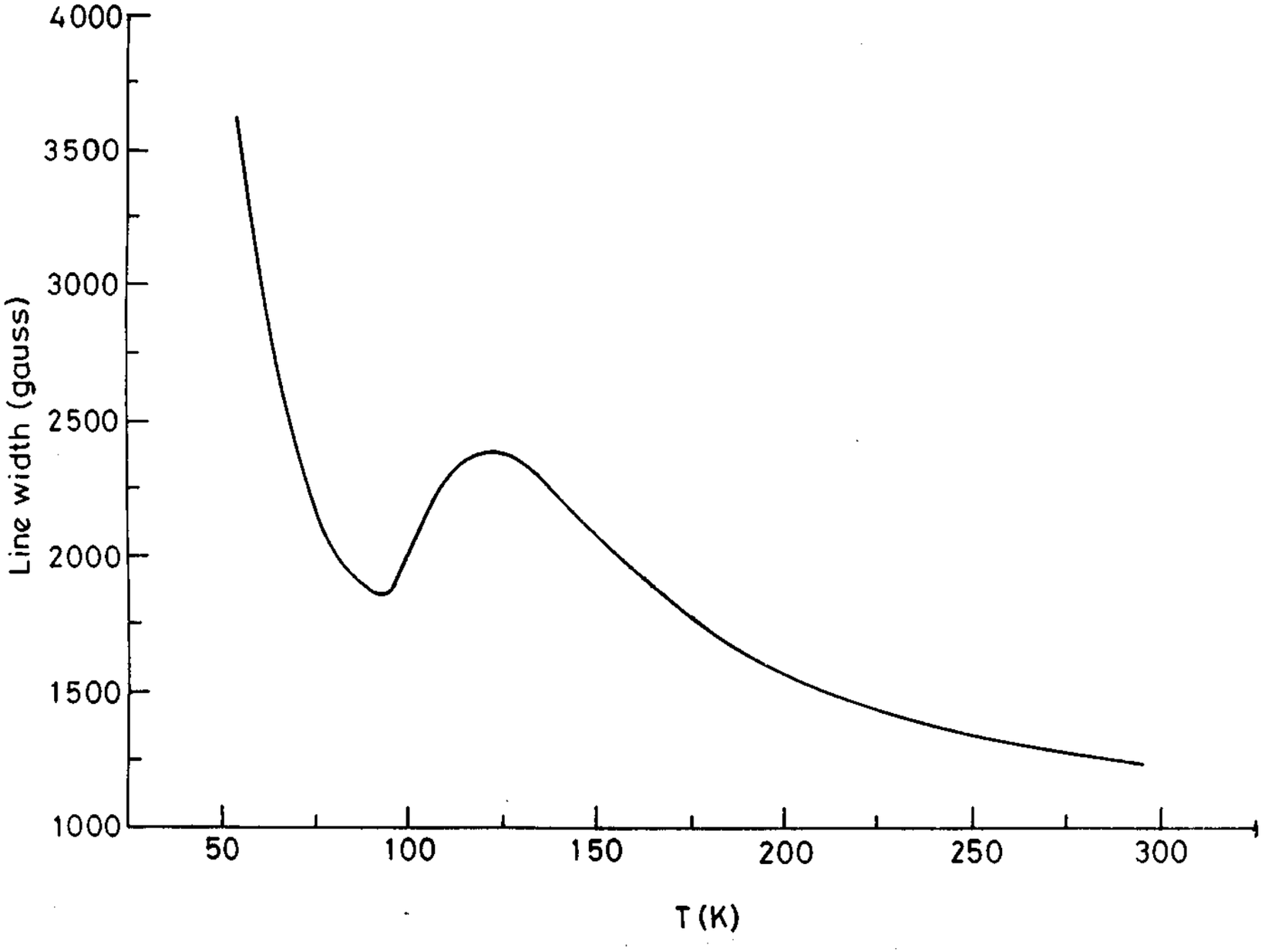

Fig.12. Variation of the ESR line width of $Gd_{0.45}Sr_{0.55}MnO_3$ with temperature.

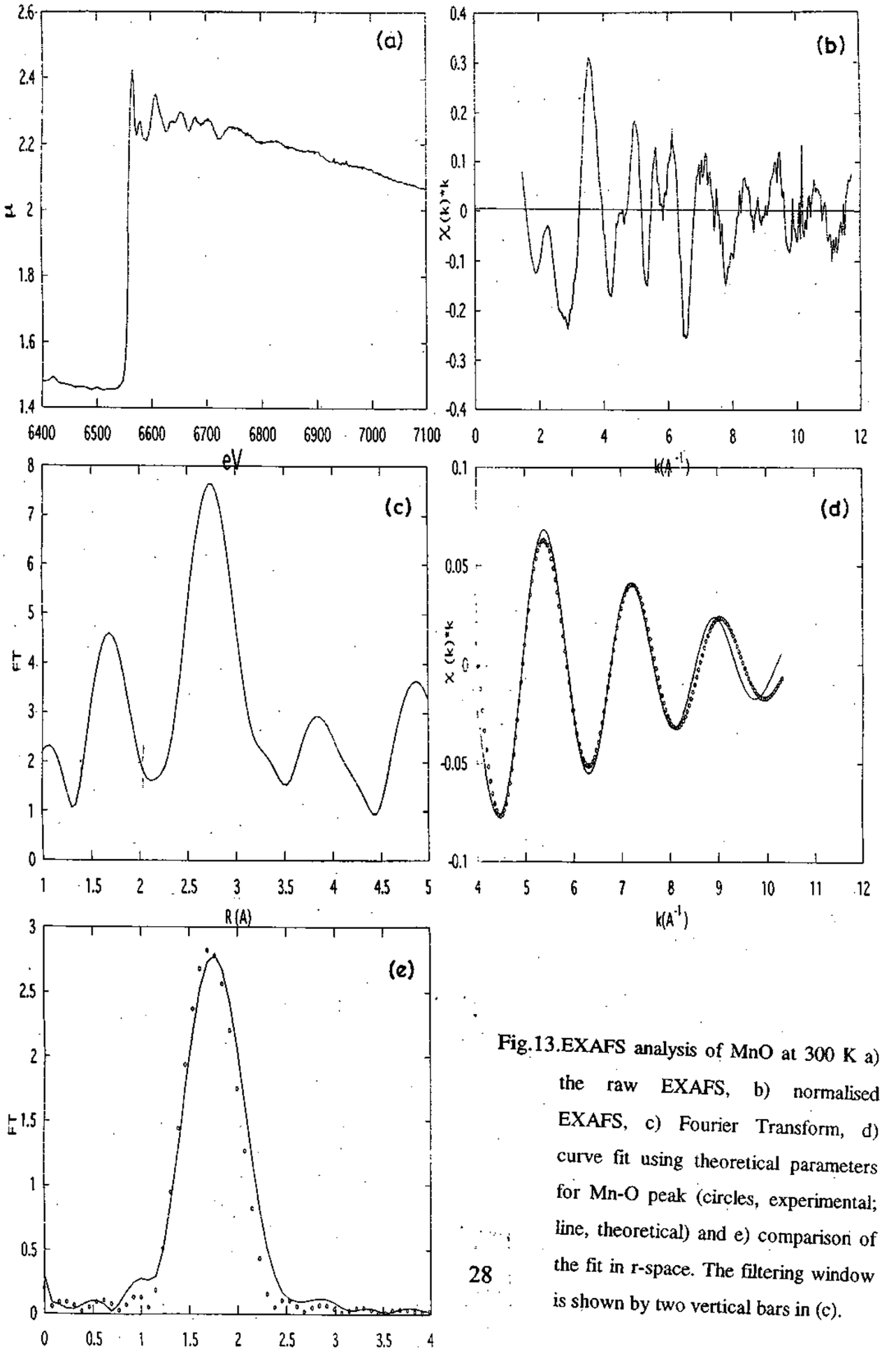

Fig.13.EXAFS analysis of MnO at 300 K a) the raw EXAFS, b) normalised EXAFS, c) Fourier Transform, d) curve fit using theoretical parameters for Mn-O peak (circles, experimental; line, theoretical) and e) comparison of the fit in r-space. The filtering window is shown by two vertical bars in (c).

Table 3

Structural Parameter obtained from EXAFS analysis

Compound	300 K				100K			
	N	R (A)	Δσ (A)	E_0 (eV)	N	R (A)	Δσ (A)	E_0 (eV)
MnO from ref. 21	6 6	2.22 2.23	0.075	-2				
$CaMnO_3$ from ref. 22	6 (2) (2) (2)	1.90 (1.895) (1.900) (1.903)	0.06	8				
$GdMnO_3$	2 2 2	1.92 1.96 2.1	0.05 0.055 0.06	13 13 13				
$YMnO_3$	2 4	2.06 2.10	0.05 0.055	17 17				
$Gd_{0.5}Ca_{0.5}MnO_3$	6	1.95	0.07	8.0	4 2	2.0 2.35	0.03 0.09	10 10
$Gd_{0.45}Sr_{0.55}MnO_3$	6	2.09	0.02	20	4 2	1.92 2.55	0 0	7 7
$Y_{0.5}Ca_{0.5}MnO_3$	2 2 2	1.95 2.03 2.1	0.03 0.04 0.04	12 12 12	2 2 2	1.89 2.21 2.56	0.07 0.03 0.08	20 20 20

crystal structure [21]. The structural parameters obtained from the EXAFS analysis are listed in Table 2. Similarly, the first prominent peaks in the FT's of $CaMnO_3$ (Fig.14) and $GdMnO_3$(Fig.15) were fitted for Mn-O coordination. The former being a pseudocubic perovskite structure could be fitted with a single distance of 1.90 Å[22], while $GdMnO_3$ required more than one set of distances to accommodate distortion in the oxygen coordination (see Table 2).

With this background, we now discuss the EXAFS results obtained with the charge ordering systems. Analysis of the EXAFS data of $Gd_{0.5}Ca_{0.5}MnO_3$ at room temperature (300 K) and at 100 K are shown in Figs.16 and 17 respectively. The Mn-O peak in the room temperature FT occurs at ~ 1.5Å and is quite broad. The inverse transformed data (R window: 1.12-1.88 Å) could be fitted with a distance of 1.95 Å for octahedral oxygen coordination. On cooling to 100 K (T_{CO} = 250 K), the FT shows remarkable changes (see Fig. 17). We now observe a peak at 1.6 Å, in addition to a shoulder on the higher R-side. Curve fitting analysis revealed the emergence of two new longer distances at ~ 2.35 Å (N ~ 2) besides the distance of ~ 2.0 Å (N ~ 4) (Table 2). Such a distribution in the Mn-O

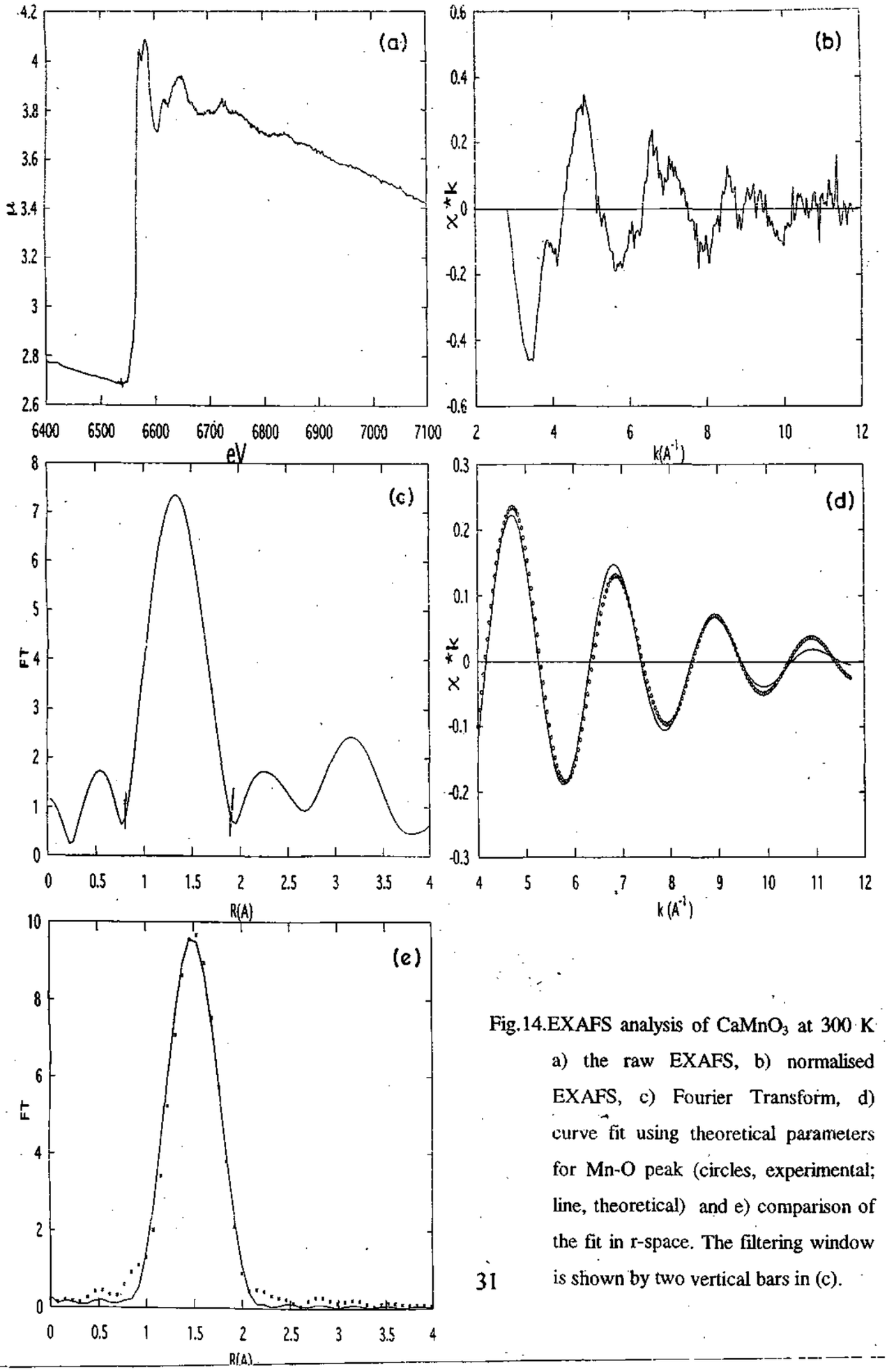

Fig.14.EXAFS analysis of $CaMnO_3$ at 300 K a) the raw EXAFS, b) normalised EXAFS, c) Fourier Transform, d) curve fit using theoretical parameters for Mn-O peak (circles, experimental; line, theoretical) and e) comparison of the fit in r-space. The filtering window is shown by two vertical bars in (c).

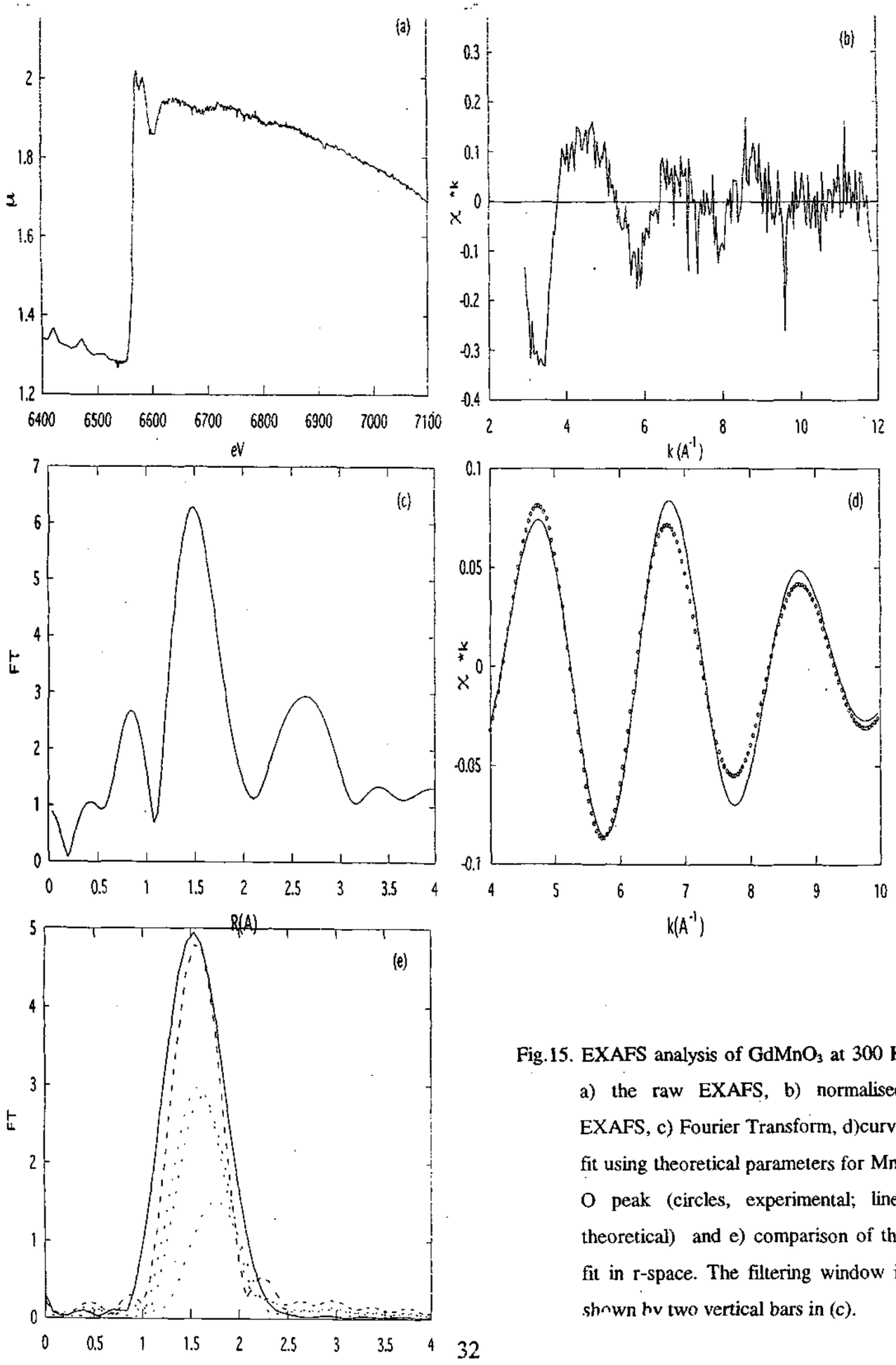

Fig.15. EXAFS analysis of $GdMnO_3$ at 300 K a) the raw EXAFS, b) normalised EXAFS, c) Fourier Transform, d)curve fit using theoretical parameters for Mn-O peak (circles, experimental; line, theoretical) and e) comparison of the fit in r-space. The filtering window is shown by two vertical bars in (c).

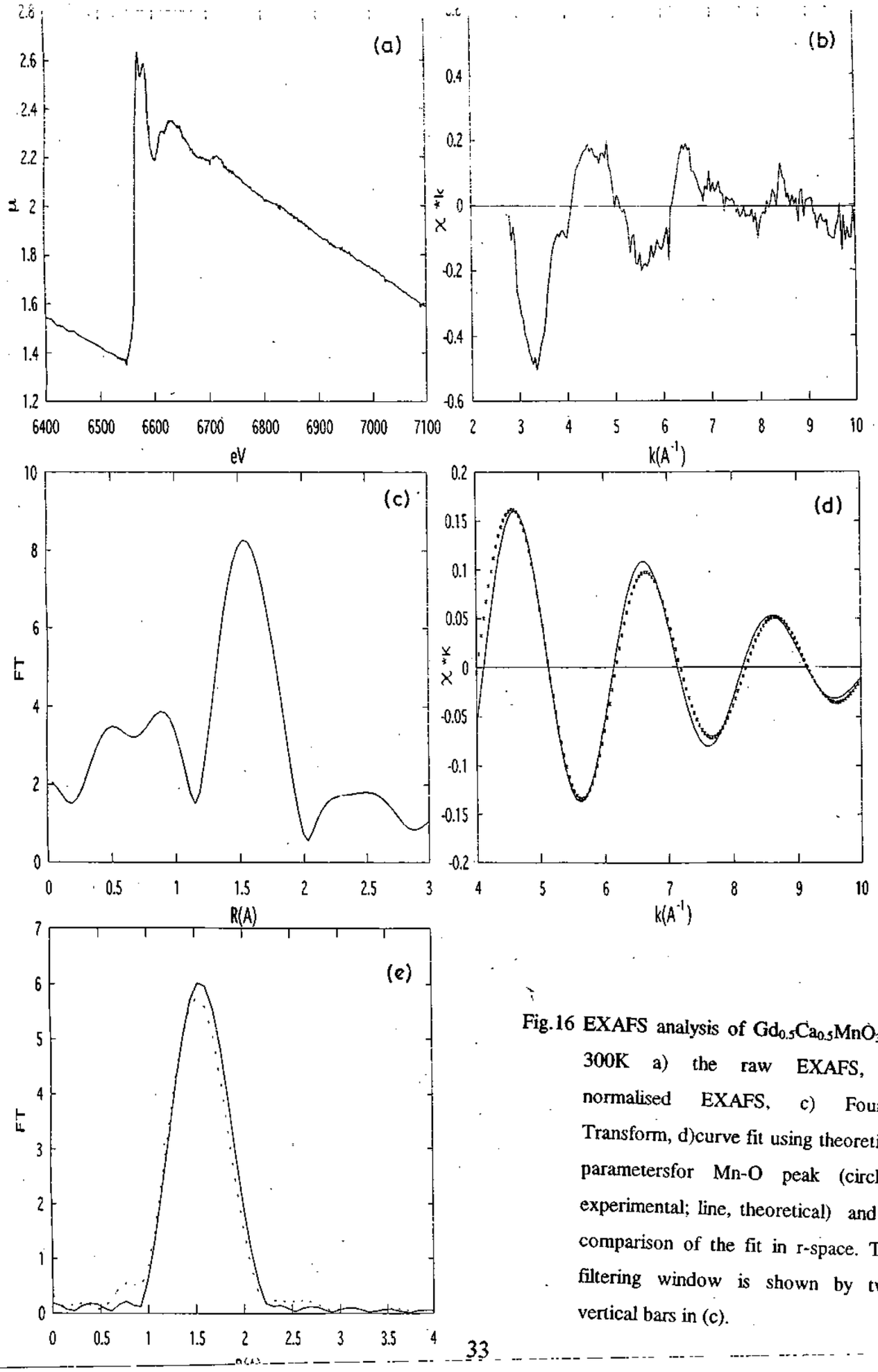

Fig.16 EXAFS analysis of $Gd_{0.5}Ca_{0.5}MnO_3$ at 300K a) the raw EXAFS, b) normalised EXAFS, c) Fourier Transform, d)curve fit using theoretical parametersfor Mn-O peak (circles, experimental; line, theoretical) and e) comparison of the fit in r-space. The filtering window is shown by two vertical bars in (c).

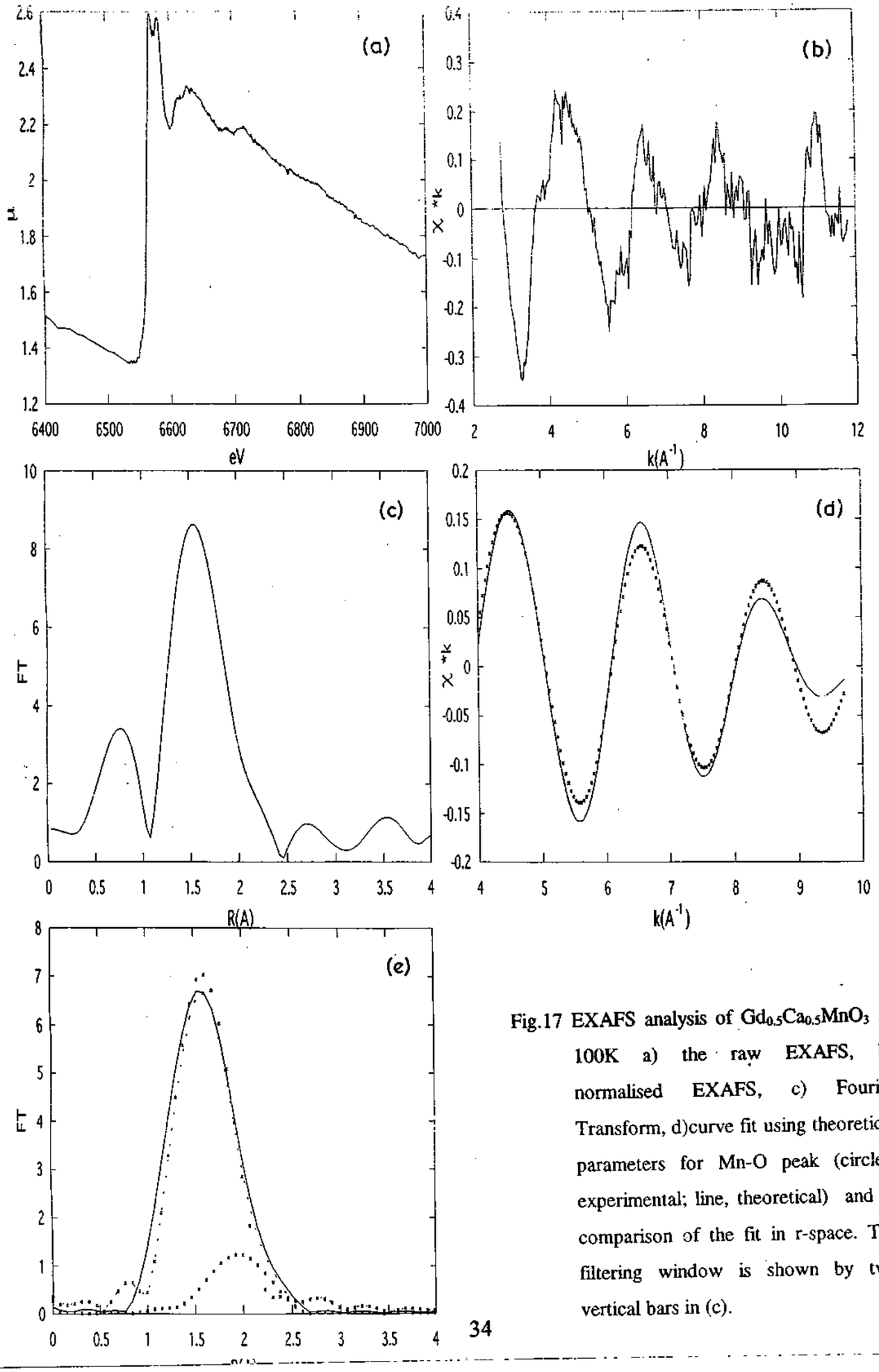

Fig.17 EXAFS analysis of $Gd_{0.5}Ca_{0.5}MnO_3$ at 100K a) the raw EXAFS, b) normalised EXAFS, c) Fourier Transform, d)curve fit using theoretical parameters for Mn-O peak (circles, experimental; line, theoretical) and e) comparison of the fit in r-space. The filtering window is shown by two vertical bars in (c).

distances appears to be related to the distorted MnO_6 octahedra at low temperatures due to charge ordering. We also notice that the Debye-Waller factors are somewhat different for the short and the long bonds probably due to the disorder.

Similar results have been obtained in the case of $Gd_{0.45}Sr_{0.55}MnO_3$ (Figs. 18 and 19). The room temperature FT (Fig. 18(c)) shows the first peak at 1.77 Å which clearly splits in two peaks 1.52 and 2.14 Å at 100 K (see Fig.19(c)). On fourier filtering, the room temperature data gave a single octahedral distance of 2.09 Å. The 100 K data on the other hand, indicated the presence of a tetragonally distorted octahedron with distances of 1.92 and 2.55 Å (Table 2).

We have extended our EXAFS work to another charge ordering system- $Y_{0.5}Ca_{0.5}MnO_3$ with T_{CO} ~ 250 K [23] (Figs.20 and 21). The room temperature FT of this compound in Fig.20c shows the first peak at 1.59 Å which on cooling to 100 K exhibits two well-defined peaks at 1.41 and 1.82 Å and a shoulder on the higher R-side. Curve fitting of the room temperature data (R-window: 1.27-2.09 Å) revealed three pairs of distances

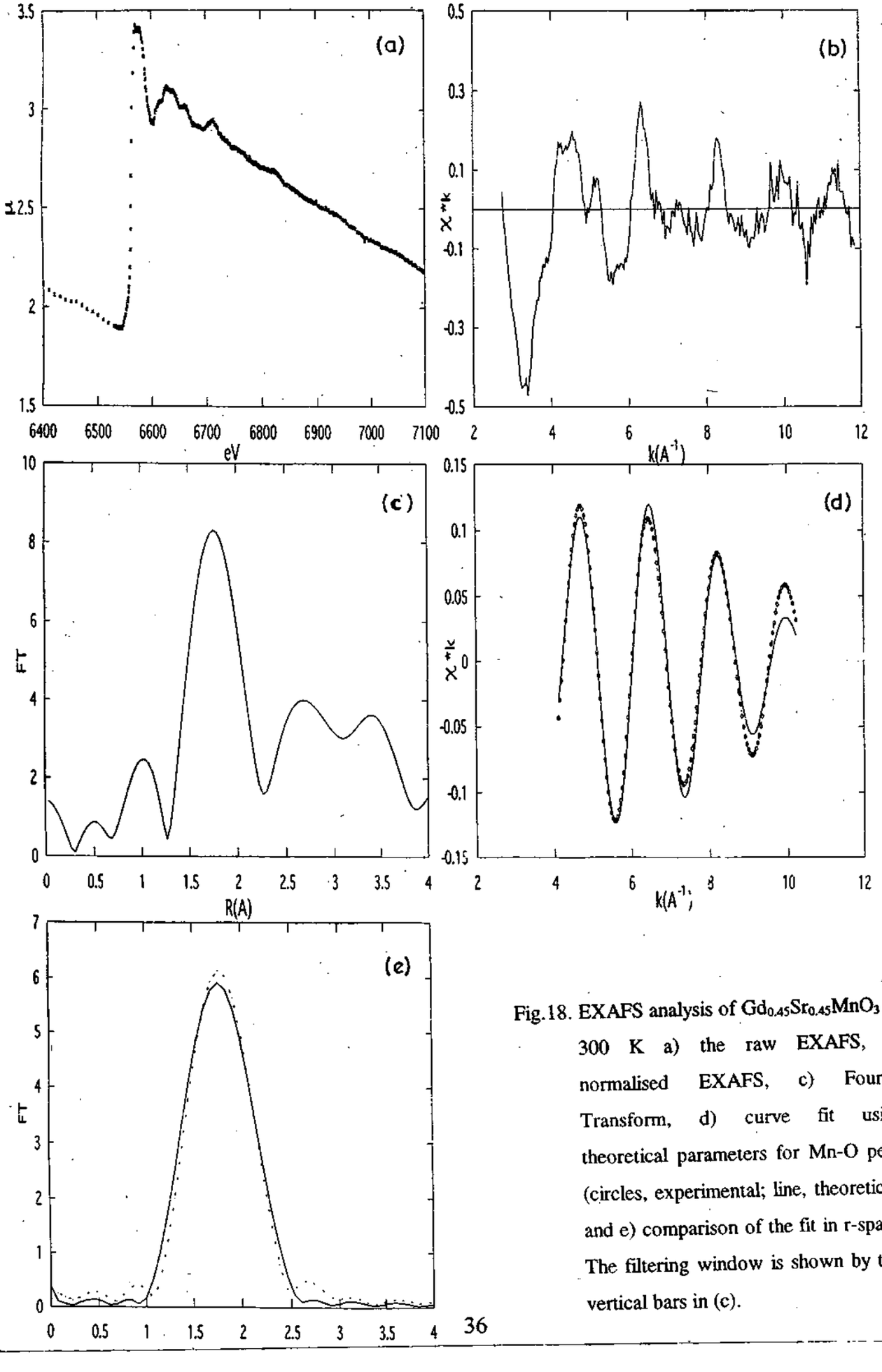

Fig.18. EXAFS analysis of $Gd_{0.45}Sr_{0.45}MnO_3$ at 300 K a) the raw EXAFS, b) normalised EXAFS, c) Fourier Transform, d) curve fit using theoretical parameters for Mn-O peak (circles, experimental; line, theoretical) and e) comparison of the fit in r-space. The filtering window is shown by two vertical bars in (c).

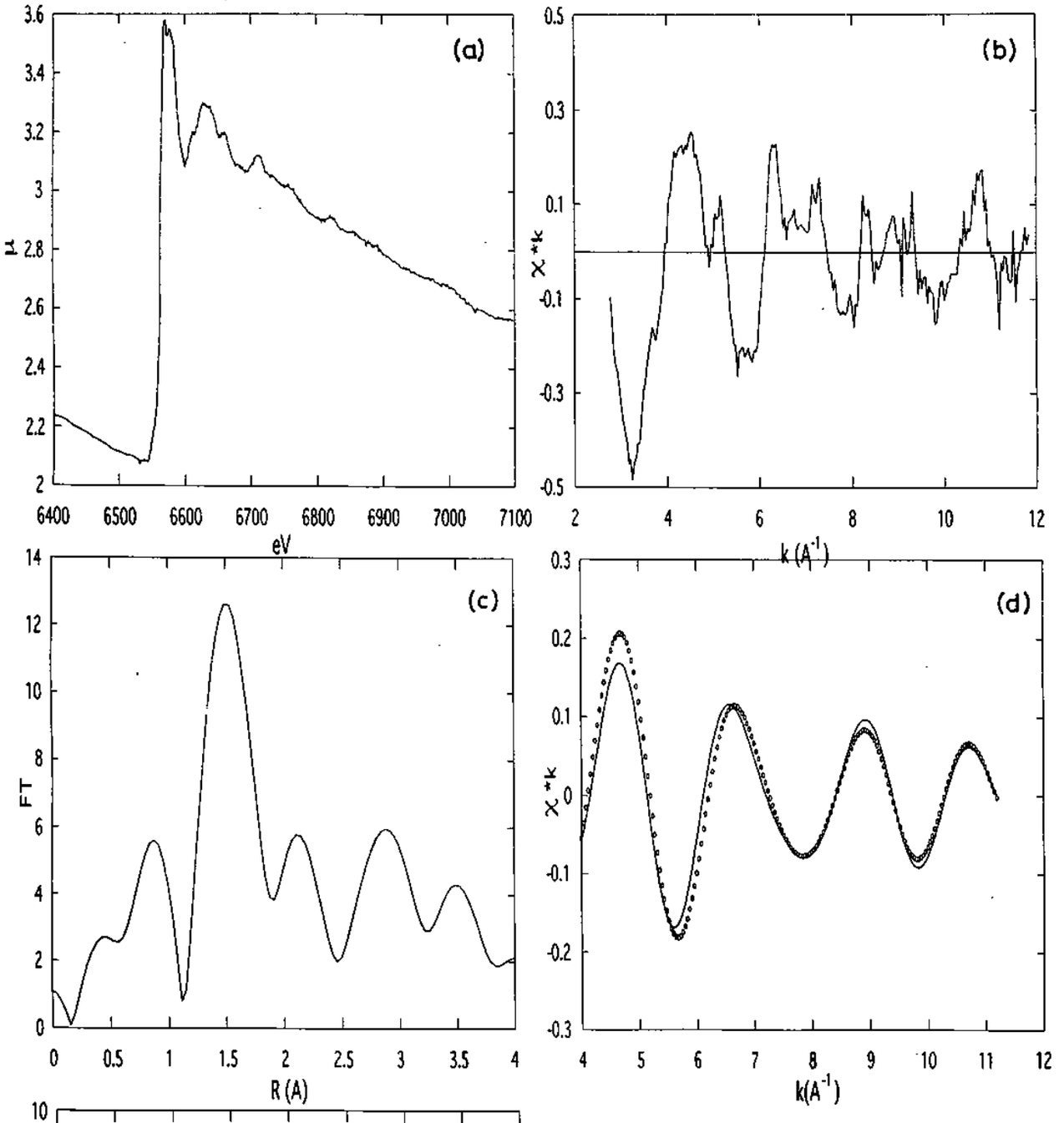

Fig.19 EXAFS analysis of $Gd_{0.45}Sr_{0.45}MnO_3$ at 100 K a) the raw data, b) normalised EXAFS, c) Fourier Transform, d) curve fit using theoretical parameters for Mn-O peak (circles, experimental; line, theoretical) and e) comparison of the fit in r-space. The filtering window is shown by two vertical bars in (c).

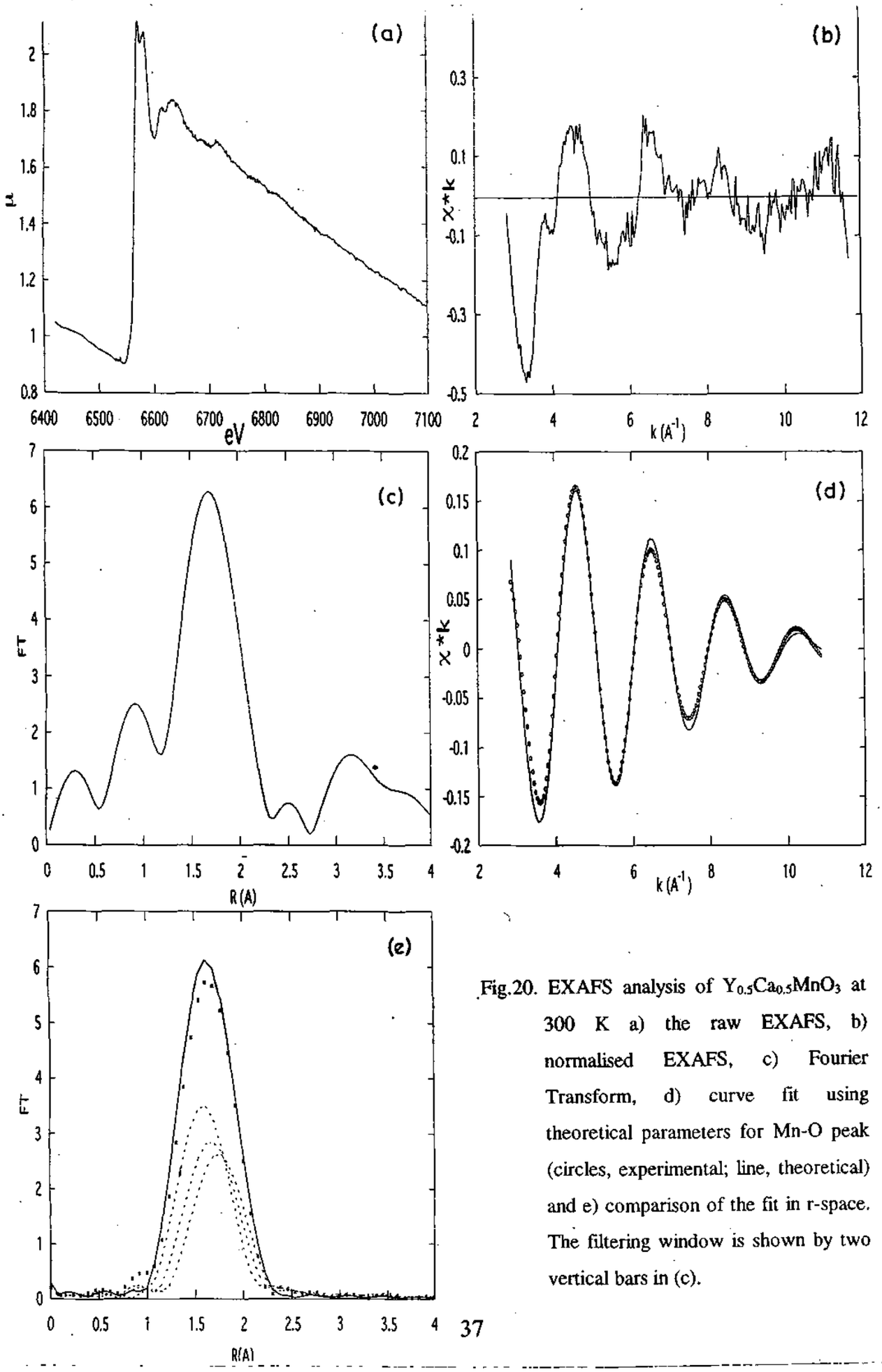

Fig.20. EXAFS analysis of $Y_{0.5}Ca_{0.5}MnO_3$ at 300 K a) the raw EXAFS, b) normalised EXAFS, c) Fourier Transform, d) curve fit using theoretical parameters for Mn-O peak (circles, experimental; line, theoretical) and e) comparison of the fit in r-space. The filtering window is shown by two vertical bars in (c).

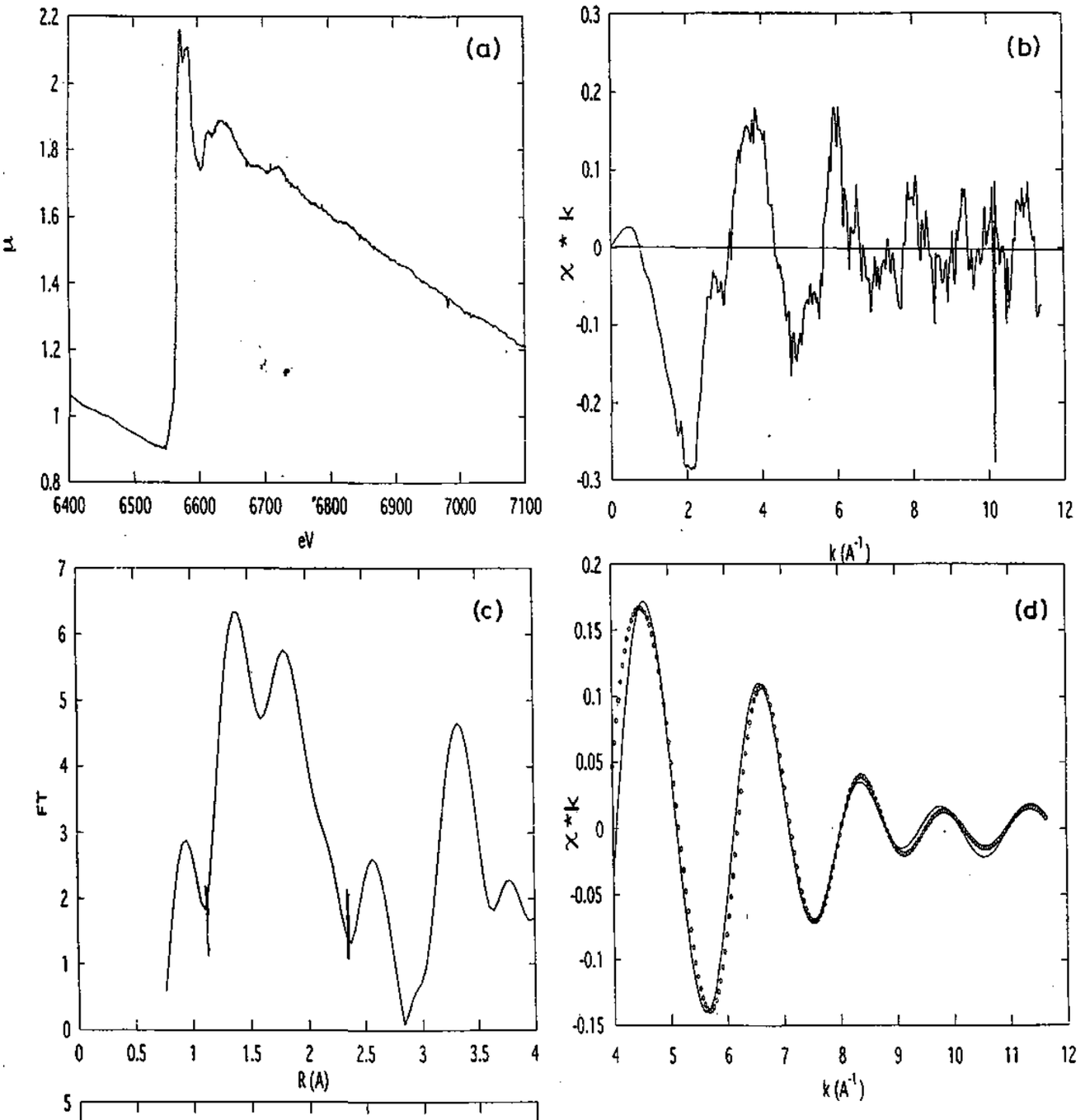

Fig.21. EXAFS analysis of $Y_{0.5}Ca_{0.5}MnO_3$ at 100 K a) the raw data, b) normalised EXAFS, c) Fourier Transform, d) curve fit using theoretical parameters for Mn-O peak (circles, experimental; line, theoretical) and e) comparison of the fit in r-space. The filtering window is shown by two vertical bars in (c).

at ~ 1.95, 2.03, and 2.1 Å, while the 100 K data gave rise to distances of 1.89, 2.21 and 2.56 Å of the tetragonally distorted octahedron.

A comment on the above observations would be in order. The charge ordered state is characterized by localized e_g electrons and therefore, the MnO_6 octahedral distortions due to the Jahn-Teller effect are static or in other words frozen below the T_{CO}. Our EXAFS measurements at 100 K have clearly shown the presence of such distortions in the octahedral oxygen coordination around Mn ions. At room temperature however, the electron hopping tends to decrease the Jahn-Teller distortions and accordingly, we observe a more regular octahedral coordination.

Effect of $\langle r_A \rangle$ on charge ordering

We show the x-ray diffraction patterns of $Pr_{0.5}Ca_{0.5-x}Ba_xMnO_3$ (x = 0, 0.125 and 0.25) in Fig.22. Phase purity of the compounds is evident as the reflections could be indexed with orthorhombic cells belonging to Pbnm space group (Table 1). The *a* and *c* parameters increase and *b*

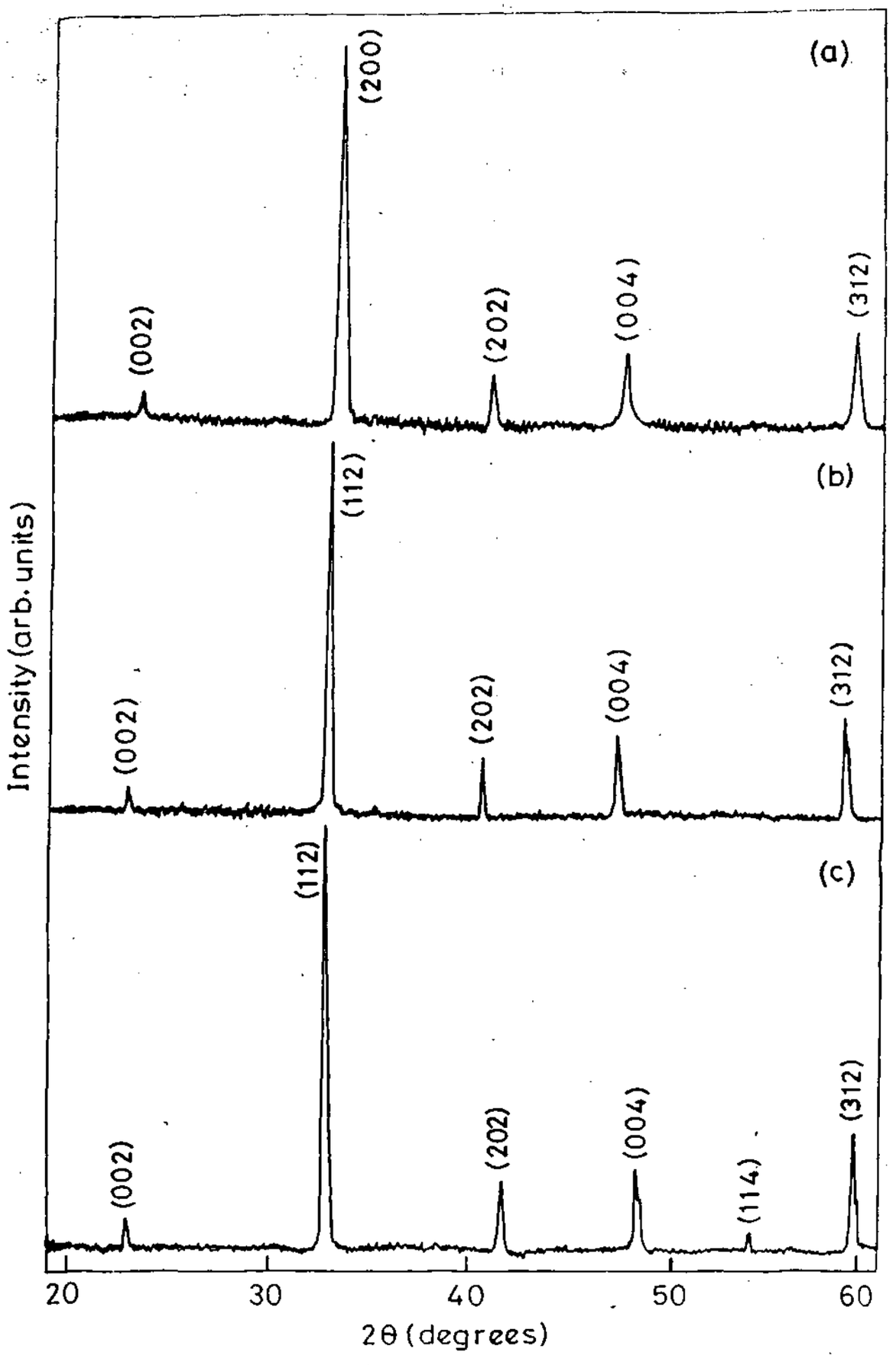

Fig.22. X-ray diffraction patterns of $Pr_{0.5}Ca_{0.5-x}Ba_xMnO_3$ a) x = 0, b) x = 0.125, c) x = 0.25.

decreases with Ba substitution while the cell volume increases from 225 to 230 $Å^3$.

Four probe electrical measurements showed all the compositions to be insulating down to 90 K as depicted in Fig.23. The data is plotted as logρ vs. 1/T in Fig.24. The curve corresponding to x = 0 composition changes its slope at ~ 200 K and that of x = 0.125 around 90 K while the x = 0.25 composition does not show any appreciable change in slope down to 75 K. The $d\log\rho/dT^{-1}$ vs. T curves in Fig.25 exhibit features corresponding to these changes. The magnetic susceptibility of $Pr_{0.5}Ca_{0.375}Ba_{0.125}MnO_3$ in Fig.26 shows two features around 260 and 90 K. It appears that the material is in a canted antiferromagnetic state at room temperature and changes gradually to antiferromagnetic state around 90 K. This transition appearing in both magnetic and electrical measurements may be due to charge ordering of the Mn ions. We note that $Pr_{0.5}Ca_{0.25}Ba_{0.25}MnO_3$ shows no such transition down to 75 K.

Pollert et al. [24] have reported T_{CO} of 253 K for the $Pr_{0.5}Ca_{0.5}MnO_3$. We find that the T_{CO} value decrease to 90 K with 25% Ba substitution in the Ca site. Higher amounts of Ba doping seem to destabilize the charge

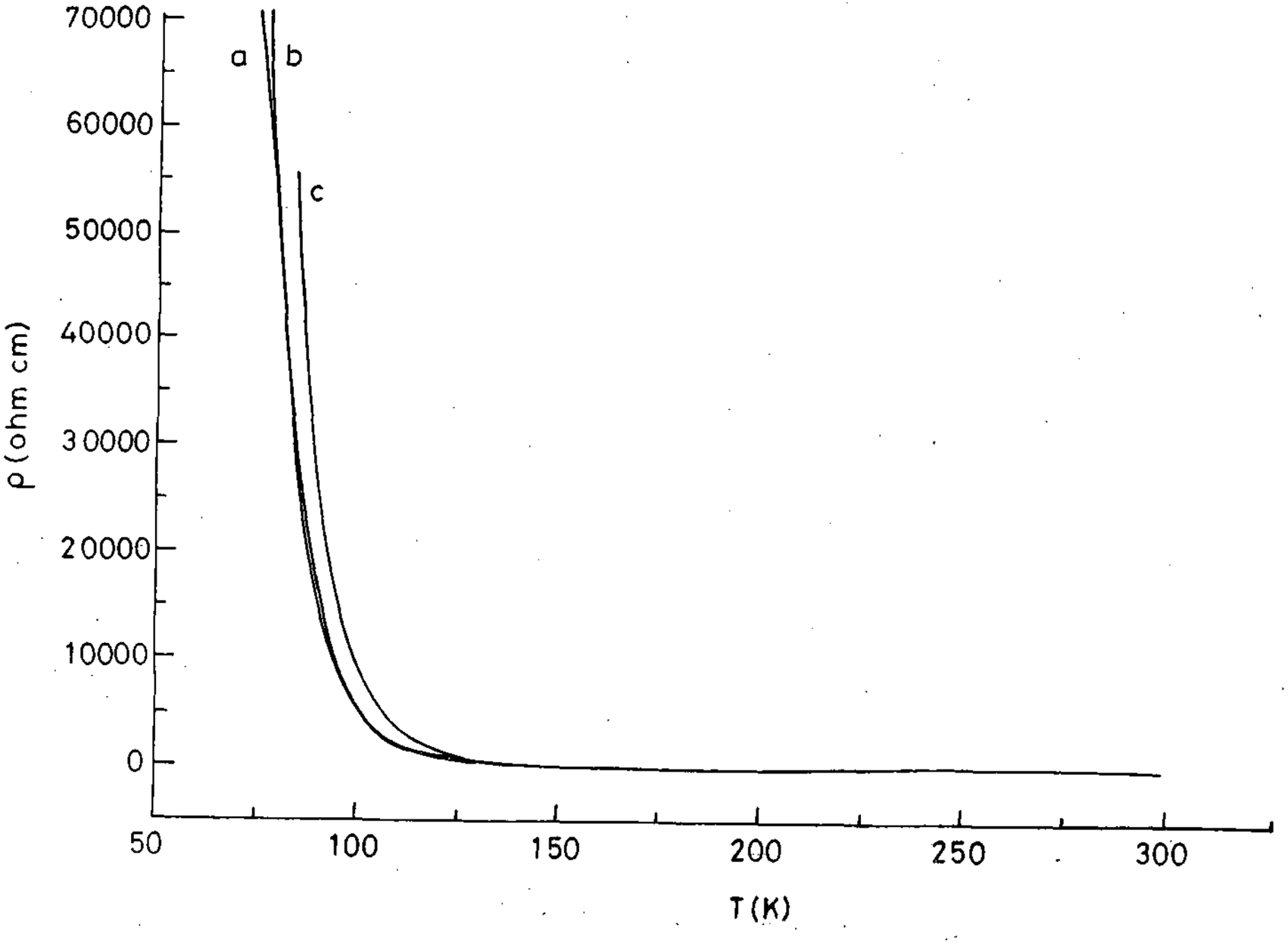

Fig:23 Temperature variation of resistivity of $Pr_{0.5}Ca_{0.5-x}Ba_xMnO_3$ a) x = 0, b) x = 0.125, c) x = 0.25.

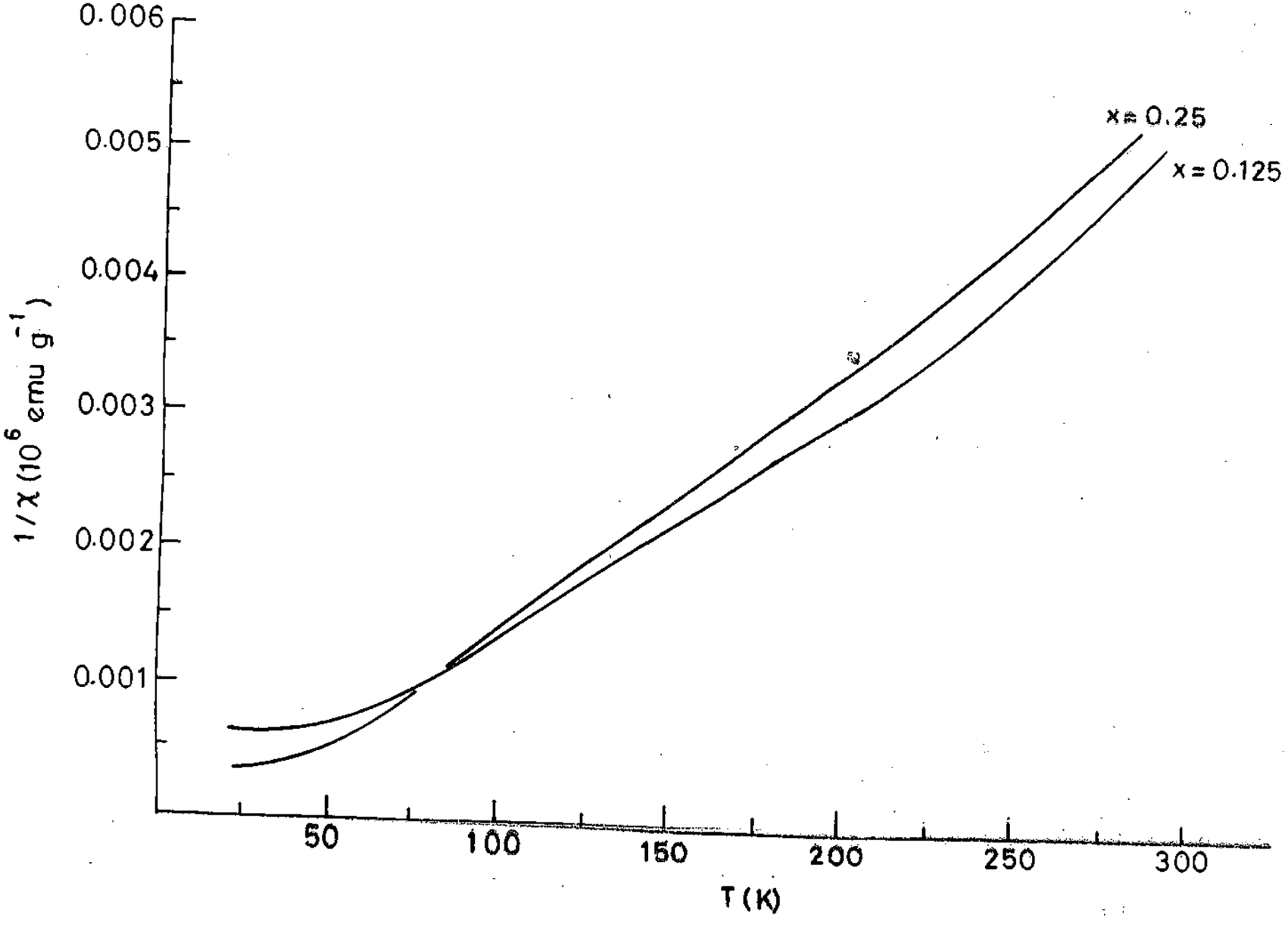

Fig.24. Variation of inverse susceptibility of $Pr_{0.5}Ca_{0.5-x}Ba_xMnO_3$ a) x = 0.125, b) x = 0.25.

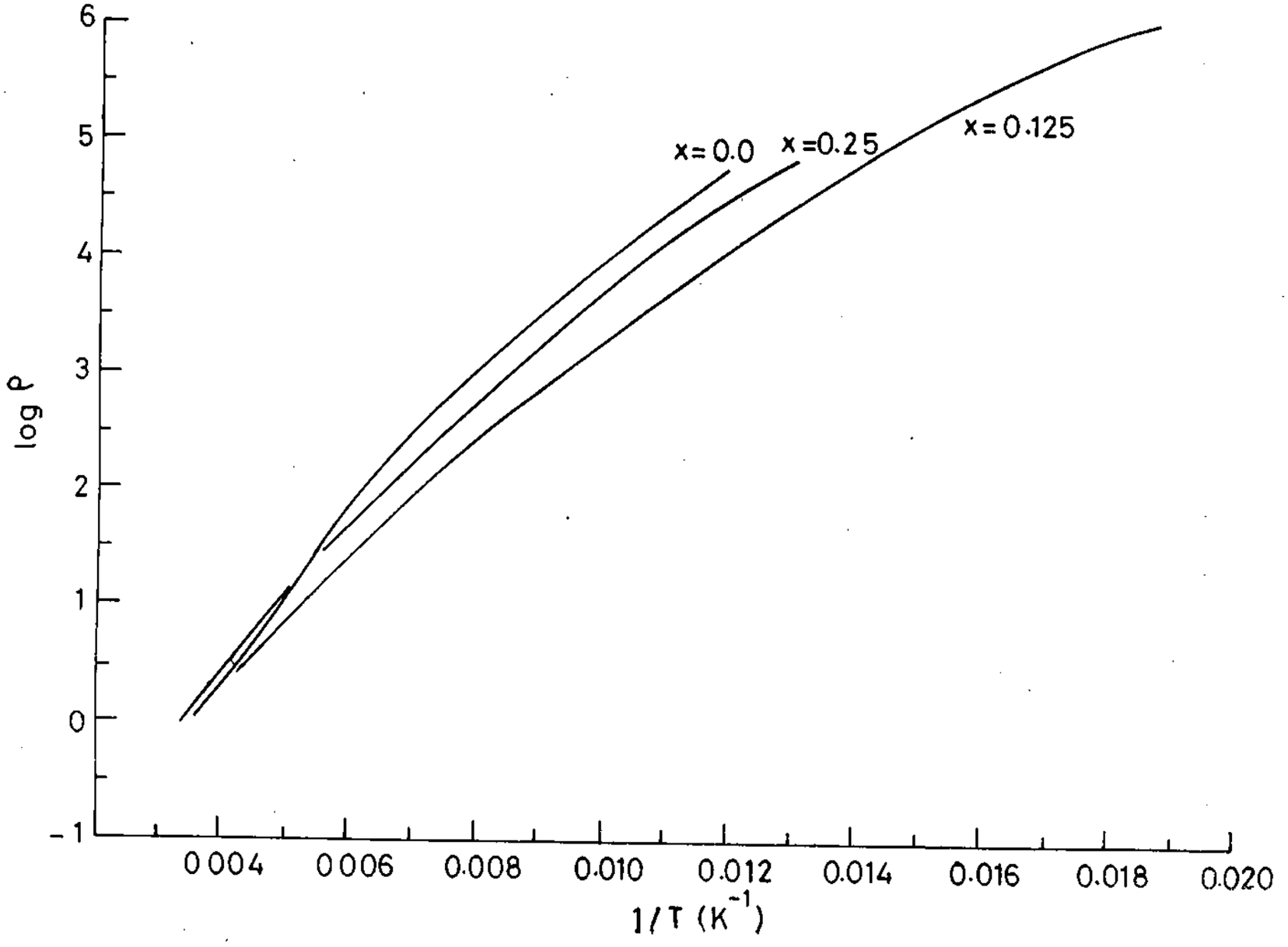

Fig.25. Variation of log (resistivity) of $Pr_{0.5}Ca_{0.5-x}Ba_xMnO_3$ a) x = 0, b) x = 0.125, c) x = 0.25 with T^{-1}.

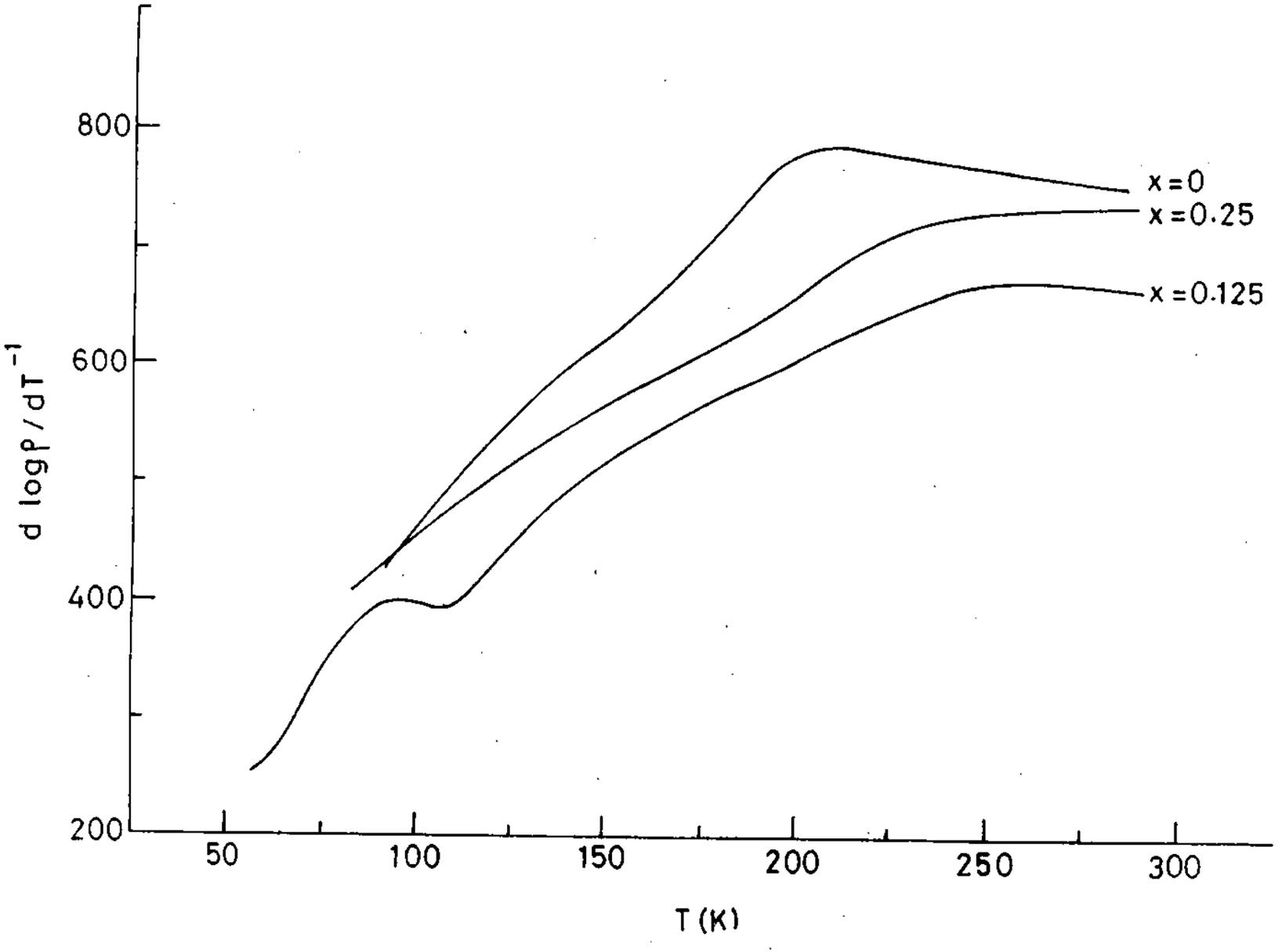

Fig.26. Variation of dlog (resistivity) / dT^{-1} of $Pr_{0.5}Ca_{0.5-x}Ba_xMnO_3$ a) x = 0, b) x = 0.125, c) x = 0.25 with temperature.

ordered state. This is really in accordance with what is expected of such a system. The $\langle r_A \rangle$ of the $Pr_{0.5}Ca_{0.5}$ system is 1.180 Å and it increases to 1.216 and 1.252 Å for Ba substitutions of 25 and 50%, respectively. From the phase diagram in Fig.4, from which we notice that the $\langle r_A \rangle$ value of the latter falls in the regime where no charge ordering occurs. The other two compositions with smaller $\langle r_A \rangle$ values however lie in the charge ordering regime. More interestingly, we find that the T_{CO} value decreases with increasing $\langle r_A \rangle$.

Conclusions

1. Static distortions of the MnO_6 octahedra due to localization of charges at low temperatures are observed using EXAFS measurements. We find four Mn-O distances ~2.0 Å and two larger distances ~2.5 Å in the compositions studied namely $Gd_{0.5}Ca_{0.5}MnO_3$, $Gd_{0.45}Sr_{0.55}MnO_3$ and $Y_{0.5}Ca_{0.5}MnO_3$ (see Table 2). At room temperature, however, we find a more regular octahedron in these compounds.

2. The charge ordering temperature, T_{CO} of $Pr_{0.5}Ca_{0.5}MnO_3$ (253 K) appears to decrease with increase in Ba substitution in the Ca site. We have related this observation to the effect of increasing $\langle r_A \rangle$ on the stability of the charge ordered state.

References

1. a) J. B. Goodenough, J.M. Longo (Au), *Landolt-Bornstein Tabellen*, Nue Series, (Springer, Berlin, 1970) Vol. III / 4a

   b) M. Rajendiran, Thesis, Indian Institute of Science, Bangalore, (1992)

   c) R. Mahesh, Thesis, Indian Institute of Science, Bangalore, (1996)

2. a) J.B.A.A. Elemans, *J.Solid State Chem.* **3**, 238 (1971).

   b) N.V. Kasper, I. O. Troyanchuk *J. Phys. Chem. Solids*, **57** , 1601 (1996).

3. a) E.O. Wollan,W.C. Koehler, *Phys. Rev.*, **100** , 545 (1955)

   b) G.Matsumoto *J. Phys. Soc. Jpn.* **29**, 606 (1970).

4. a) P.W. Anderson, H. Hasegawa, *Phys. Rev.* **100**, 675 (1955).

   b) J.B. Goodenough, *ibid.* **100**, 564 (1955).

   c) J. Kanamori, *J.Phys. Chem. Solids.* **10**, 87 (1959).

5. R. Pauthnet, C.Veyret, *J. de Phys. (Paris).* **31**, 65 (1970).

6. a) M.Verelst, N.Rangavittal, C. N. R. Rao, A. Rousset, *J. Solid State Chem.* **104**, 74 (1993).

   b) R. Mahesh, K. R. Kannan, C. N. R. Rao, *ibid.* **114**, 294 (1995).

7. R. Mahendiran, R. Mahesh, N. Rangavittal, S. K. Tewari,
A. K. Raychaudhuri, T. V Ramakrishanan, C. N. R. Rao,
Phys. Rev. **B56**, 3348 (1996).

8. K. Chahara, T. Ohno, M. Kasai, Y. Kozono, *Appl. Phys. Lett.*
63, 1990 (1993).

9. a) R. Von Helmolt, B. Holzapfel, L. Schultz, K. Samwer,
Phys. Rev. Lett. **73**, 2331 (1993).
b) M. McCormack, S. Jin, T. Tiefel, R. M. Fleming,
J. M. Phillips, R. Ramesh, Appl. *Phys. Lett.* **63**, 1990 (1993).
c) R. Mahesh, R. Mahendiran, A. K. Raychaudhuri, C. N. R. Rao, *J.*
Solid State Chem. **114**, 297 (1995).
d) C. N. R. Rao, A. K. Cheetham, *Science* **272**, 369 (1996).

10. A. Urishibara, Y. Morimoto, T. Arima, A. Asamitsu, G. Kido,
Y. Tokura, *Phys. Rev.* **B51**, 14103 (1995).

11. a) G. H. Jonker, J. H. Van Santen, *Physica,* **16**, 377 (1950).
b) J. H. Van Santen, G. H. Jonker, *ibid.* **16**, 599 (1950).

12. C. Zener, *Phys. Rev.* **82**, 403 (1951).

13. J.B. Torrance P. Laccore, A. I Nazzal, E. J. Ansaldo, CH. Niedermayer,
Phys. Rev. **B45**, 8209 (1992).

14. C. N. R. Rao. *Chem. Eur J.* **2**, 1499 (1996).

15. Y. Tomioka, A. Asamitsu, Y. Moritomo. H. Kuwahara, Y. Tokura, *Phys. Rev. Lett.* **74** , 5108 (1995).

16. Y. Tokura, Y. Tomioka, H. Kuwahara, A. Asamitsu, Y. Morimoto, M. Kasai, *J. Appl. Phys.* **79**, 5288 (1996).

17. T. Vogt, A. K Cheetam, R. Mahendiran, A. K Raychaudhri, R. Mahesh, C. N. R. Rao, *Phys. Rev.* **B54**, 15303 (1996).

18. T. A Tyson, J. Mustre de Leon, S.D. Conardson, A.R. Bishop, J. Neumeier, H. Roder, Jun Zang *Phys. Rev.* **B53**, 13985 (1996).

19. A. I. Vogel`s *Text book of Quantitative Chemical Analysis*, ELBS, Longman Group UK Ltd., (1994)

20. A. Michalowich, EXAFS pour le MAC, in `Logicles pour la chime', societe' Francise de Chimie, Paris (1991), p.102.

21. B. Morosin, *Phys. Rev.* **B1**,236 (1970).

22. K. R. Poeppelmeier, M. E. Leonowicz, J. C. Scanlon, J. M. Longo, W. B. Yelon *J. Solid State Chem.* **45**, 71 (1982).

23. A. Arulraj, R. Gundakaram, N. Rangavittal, N. Gayathri, A. K. Raychaudhri, C. N. R. Rao (communicated)

24. E. Pollert, S. Krupicka, E. Kuzmicova *J. Phys. chem. solids*, **43**, 1137 (1982).

PART II

SYNTHESIS AND CHARACTERIZATION OF PVP STABILIZED AND CLAY INTERCALATED METAL NANOPARTICLES

Introduction

Particles of diameters between 1-50 nm constitute nanoclusters. Physical properties of such clusters correspond neither to those of free atoms (molecules) nor to those of bulk solids with the same chemical composition. These clusters are characterized by a large surface area to volume which implies that a large number of atoms reside at the surface[1].

Fine metal particles with controlled size and shape find extensive applications in several fields. For instance, nanosized ferromagnetic particles are used for high density recording while precious metal particles are used for making conducting inks and pastes in electronic industry[2,3]. Metal powders having required characteristics can be prepared by various physical, chemical and electrochemical methods. Of the chemical methods, the most frequently used involve the reduction of metallic compounds

followed by precipitation from the homogeneous solution. In order to get small particles with narrow size distribution, the growth of these particles have to be inhibited, which can be done either by using a surfactant like polyvinyl pyrrolidone (PVP)[4] or by using a host lattice like montmorillonite[5] during the reduction process. The interparticle interactions therefore decrease due to the chemical coating of the surface[6]. In the case of host lattices, it is the pore size[7] that sterically restricts the growth of the particle, resulting in small, monodisperse metal particles. For example, the clay-montmorillonite has a two dimensional layered alumino silicate structure[8], with exchangeable cation between the layers. Cations to be reduced can be exchanged with the interlayer cations. In this case, the interlayer spacing (~ 5Å) tends to constrain the particle size[5].

We have prepared various metal nanoparticles (Au, Ag and Cu) using polyols as the reducing agents in the presence of PVP and Ag in the presence of montmorillonite.

Experimental

In the first method using PVP, nanoparticles of silver were prepared with ethanol as the reducing medium instead of polyol[4]. In this process, a known quantity of silver nitrate was taken in 100 ml of ethanol containing a predetermined quantity of polyvinyl pyrrolidone (PVP). The ethanolic solution containing silver nitrate and PVP was refluxed (~ 360 K) under stirring conditions for a period of 12h. This resulted in the formation of silver nanoparticles. Similar methods of preparation were used to form Cu, and Au nanoparticles using copper acetate and chloroauric acid as precursors. Even though this procedure was successful in yielding nanoparticles of Ag, in the case of Cu and Au it required addition of one equivalent of magnesium metal powder (relative to the metal salt) in order to facilitate the reduction. Here, Mg acts as a reducing agent[10] and in the course of reaction ethanol gets oxidized to acetaldehyde and other products.

In the second method, silver nanoparticles were obtained dispersed on Na-montmorillonite. The structural formula of the

montmorillonite is $(Na_{0.33}K_{0.01}Ca_{0.02})_4(Al_{1.6}Fe_{0.08}Mg_{0.32})(Si_{3.89}Al_{0.11})O_{10}(OH)_2.nH_2O$ whose cation exchange capacity and mean particle size were measured to be 112 m.eq / 100g and $< 2\mu$ respectively. Various amounts of $AgNO_3$ (ratio of the weight percentage of clay to silver nitrate was 1:0.1, 1:0.25, 1:0.5, 1:1 and 1:3) were introduced in the interlayer of montmorillonite by treating the clay with silver nitrate solution. The vessel was wrapped in black paper in order to prevent the darkening of silver due to light, the mixture was stirred at room temperature for 24 h. The suspension was filtered, washed repeatedly with distilled water until no silver ions were detected in the filtrate, which was tested using dil.HCl solution.

In order to facilitate reduction, about 1g of $AgNO_3$ interlayered montmorillonite was suspended in 100g of ethylene glycol in a three necked RB flask and refluxed at 180° C for 2 h in N_2 atmosphere (nickel acetate montmorillonite was refluxed for 24 h). The solid recovered after reduction by suction was washed with methanol and dried in a dessicator. The reduced samples were first washed with nitrogen purged water, then with methanol and vacuum dried.

Elemental Analysis

The samples prepared by the latter method were analysed for their constituent elements according to the following procedure. The samples subjected to ethylene glycol reduction and subsequent washing were ashed at 900 C in a platinum dish. A known quantity (150 mg) of the ashed sample was dissolved in 10 ml of HF, 10 ml of Conc.HNO_3, and 10 ml of de-ionized water in a platinum crucible and gently heated to dryness. The dried residues were then redissolved in a mixture of 10 ml Conc.HNO_3 and 10 ml of water and made up to a known volume. The amount of silver present was determined by atomic absorption spectroscopy which was calibrated using standard solutions of silver.

The samples thus prepared were characterized using XRD, elemental analysis, TEM and electric and magnetic measurements (in the case of Ni). X-ray diffraction patterns were recorded using a JEOL diffractometer. Specimens for TEM were prepared by dispersing a few micrograms of the powdered samples in one drop of isopropyl alcohol placed on carbon coated grids, followed by evaporation of the alcohol.

A JEOL (200 kV) electron microscope was employed for the above study. Mean particle size was calculated by making histograms from the TEM images. The average particle size has also been calculated from the XRD pattern using Scherrer's formula

$$t = 0.9\lambda / B\cos\theta_B$$

where t is the average particle size

λ is the wavelength of the X-ray used

θ_B is the Bragg angle

B is the broadening which is measured in radians using Warren's formula

$$B^2 = B_M^2 + B_S^2$$

where B_M and B_S are the full width at half maximum of the peak under consideration and of the standard (KCl) respectively.

Results and discussion

a) Nanoparticles prepared using PVP as the protective agent

Reduction of $AgNO_3$ by ethanol in the presence of PVP gave nice colloidal solutions of very small particles in the nanometric range.

In Fig.1, we show the TEM images of silver nanoparticles obtained by employing $AgNO_3$ ratios of 1:5 and 1:10. Along with the micrographs we have provided the histograms showing the particle size distributions. For $AgNO_3$:PVP ratio of 1:10, we see that the particles are small with a narrow size distribution, the mean diameter being ~5nm. For $AgNO_3$:PVP ratio of 1:5, we obtain Ag particles with a mean diameter of 13-15 nm. The particle size distribution is clearly sensitive to the concentration of PVP. It may be noted that refluxing $AgNO_3$ in the absence of PVP did not yield nanoparticles. We could not record the XRD patterns of the Ag particles because the nanoparticles were finely dispersed in colloid form in the solution. Electron diffraction patterns however show the FCC structure of Ag. The absorption band of the colloidal solution was found to be around 415 nm. This is characteristic of the plasmon band of Ag colloid[4, 10].

Refluxing $HAuCl_4$ in ethanol in the presence of PVP, did not yield Au nanoparticles. However on refluxing $HAuCl_4$ with ethanol/PVP mixture in the presence of magnesium (one equivalent with respect to $HAuCl_4$), we could obtain fine nanoparticles. In Fig. 2

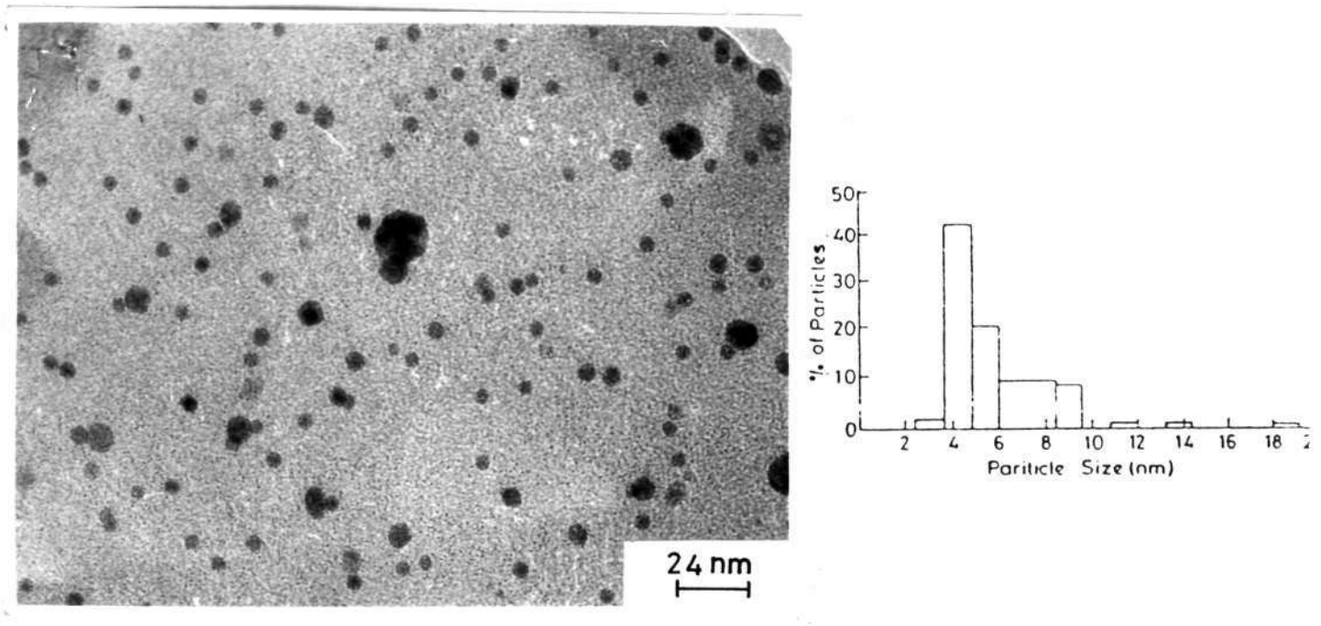

Fig. 1. Transmission electron micrographs of silver nanoparticles (1:10) along with the histograms showing particle size distributions

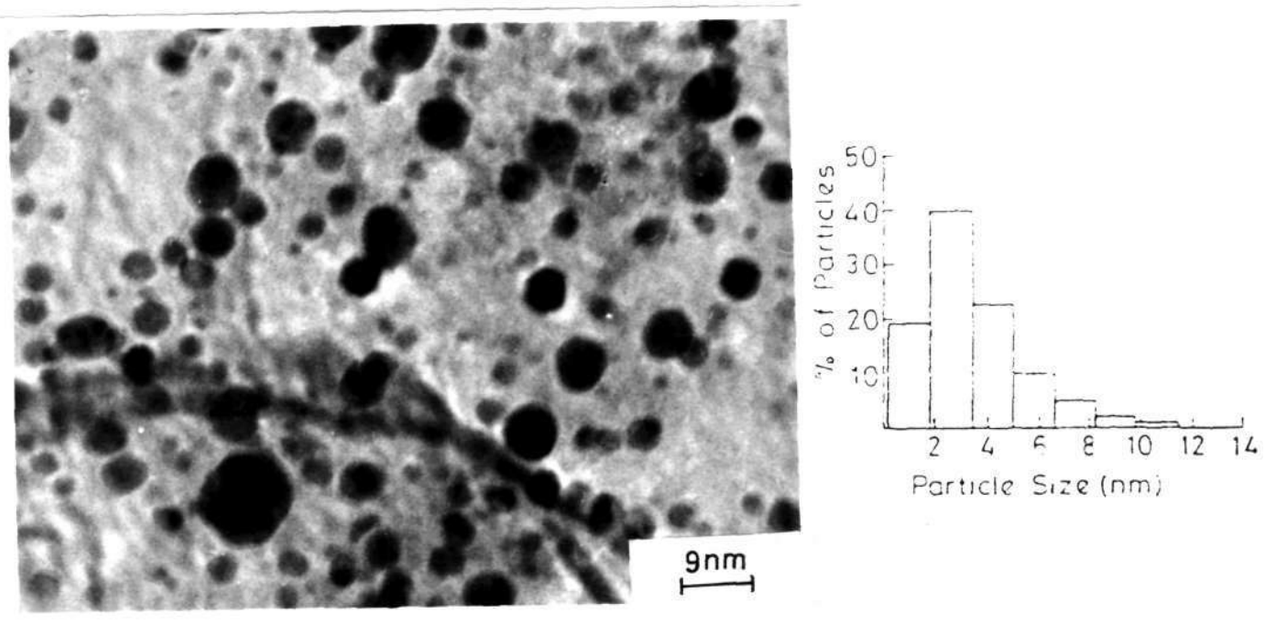

Fig. 2. Transmission electron micrograph of gold nanoparticles along with the histogram showing the particle size distribution (1:10 sample).

we show a TEM image of the Au nanoparticles (obtained with a $HAuCl_4$:PVP weight ratio of 1:10) along with a histogram giving the particle size distribution. The mean particle size is 5nm. The TEM image of the particles obtained with $HAuCl_4$:PVP weight ratio of 1:5 gave a mean particle size of 12nm. The particle size distribution of the Au nanoparticles is sensitive to the PVP concentration, just as in the case of the Ag particles. The XRD pattern in Fig.3 clearly indicates the crystalline nature of the Au nanoparticles. The particle size obtained from the x-ray line broadening was 18nm.

Our attempts to prepare Cu nanoparticles by refluxing copper acetate in ethanol in the presence of PVP were not successful. The reaction always gave copper oxides. However addition of one equivalent of magnesium metal to the reaction mixture (as in the case of preparation of Au nanoparticles), lead us to metallic Cu particles. These preparations were carried out in a pure nitrogen atmosphere to minimize the oxide formation. The TEM image of Cu particles obtained with a copper acetate:PVP ratio of 1:10 is shown in Fig.4. We do not see well separated copper nanoparticles extensively. There are

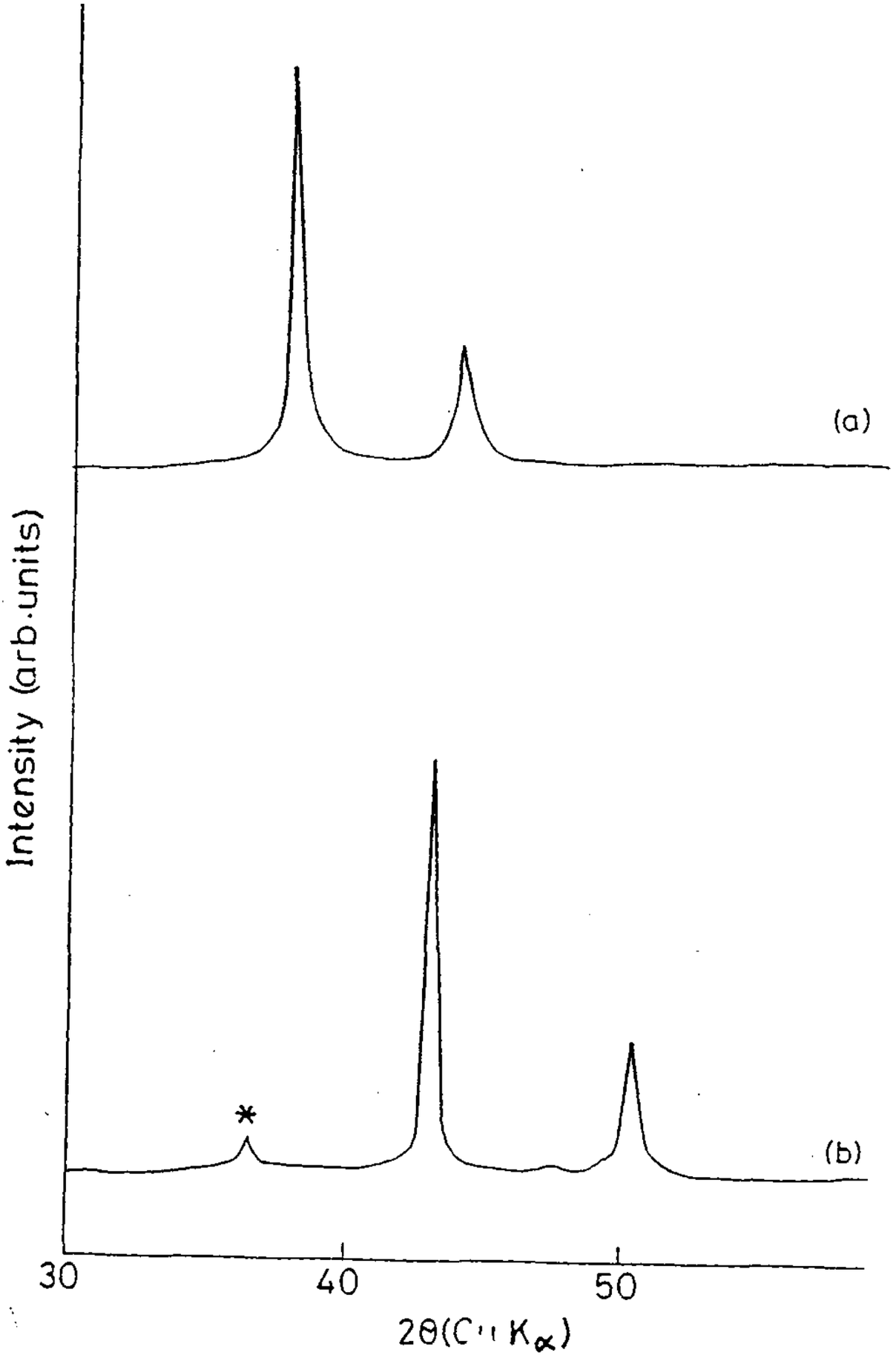

Fig. 3. X-ray diffraction patterns of the nanoparticles of (a) gold (1:5) and (b) copper (1:10).

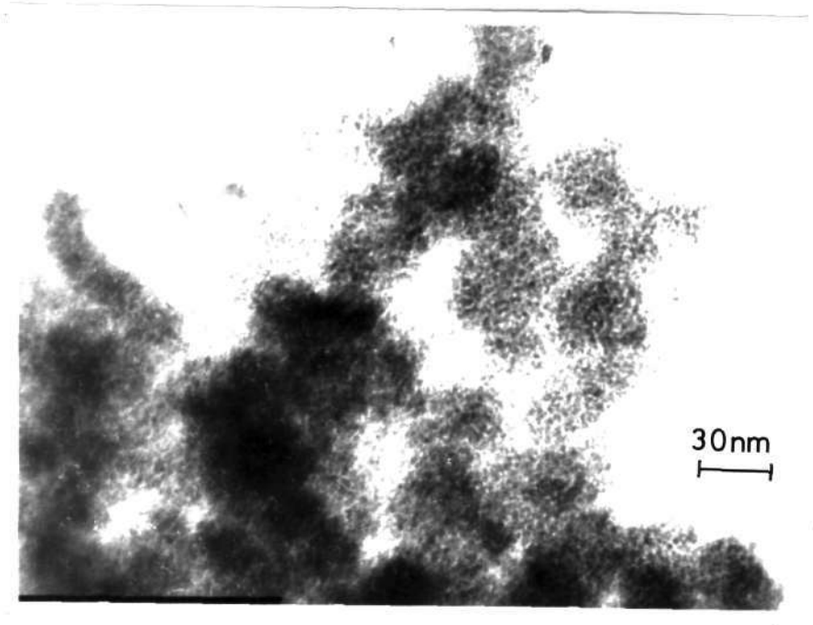

Fig. 4. Transmission electron micrograph of copper nanoparticles (1:10 sample).

some isolated nanoparticles of 5-10nm diameter, but most of the metal particles are loosely clustered giving rise to particles in the 20-100nm range. The XRD of these particles is shown in Fig.3. The reflections due to copper oxide impurity is marked with an asterix. The particle diameter estimated from the x-ray line broadening is 21nm.

b) Nanoparticles prepared using montmorillonite as a host material

X-ray diffraction patterns of the dried montmorillonite interlayered with varying amounts of silver nitrate is shown in Fig.5 along with the pattern of the parent clay for the purpose of comparison. We see that the XRD patterns of clay change with the clay to silver ratio. As can be seen from the figure, the (002) peak intensity increases with respect to the I(001), with the increasing content of $AgNO_3$. The relative intensities of the first and the second order reflections are indicative of the extent of inter layering. The d(001) of the clay increases after the exchange from 9.8 Å to 14.98 Å. On subjecting these samples to ethylene glycol reduction the d(001) value changes from 14.98 to 14.85 Å Fig.6 . We notice that the (001) reflection becomes more intense than the (002) reflection and the (111), (002)

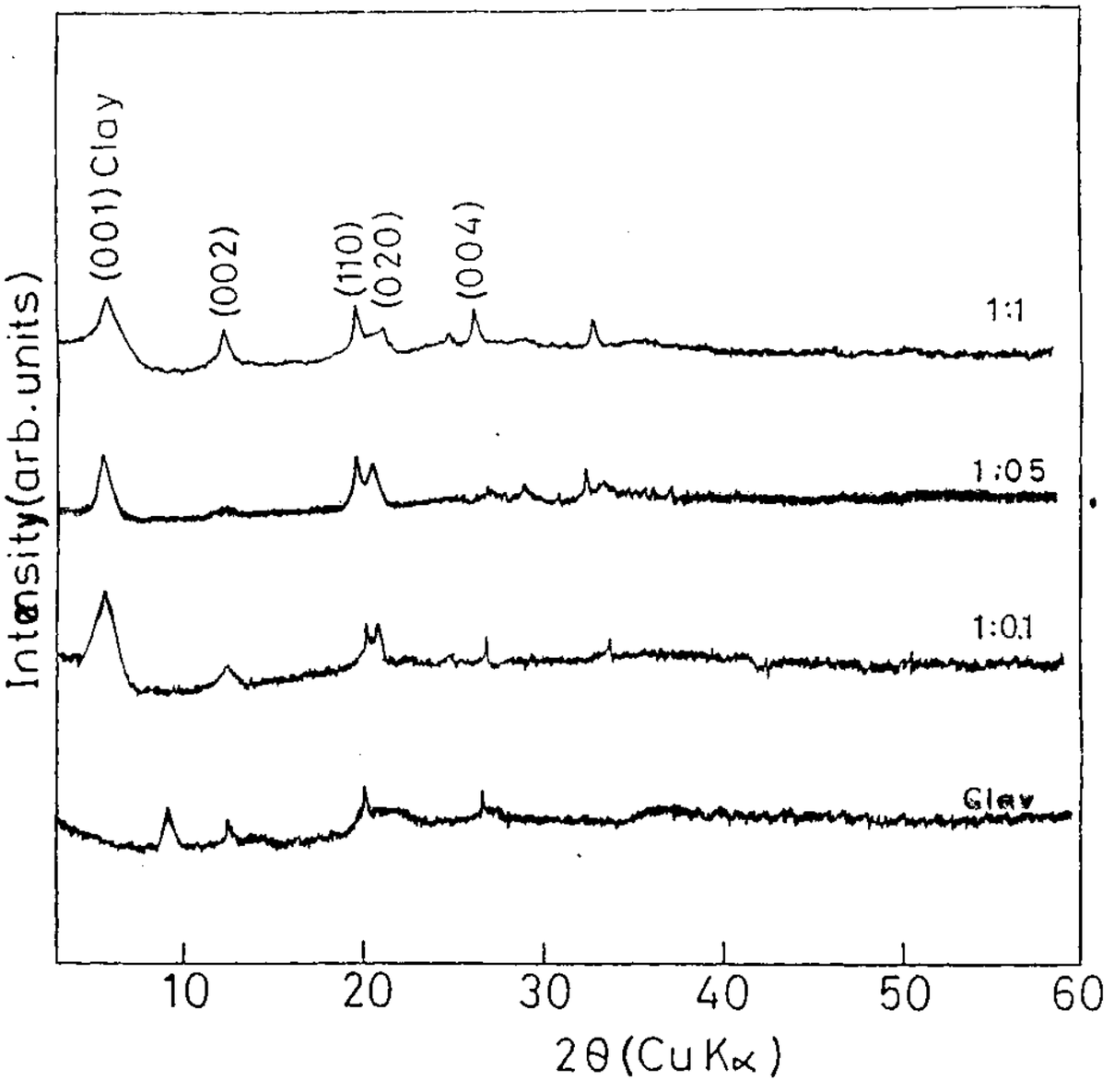

Fig. 5. X-ray diffraction patterns of dried montmorillonite intercalated with $AgNO_3$. The weight ratios of clay to silver nitrate are shown.

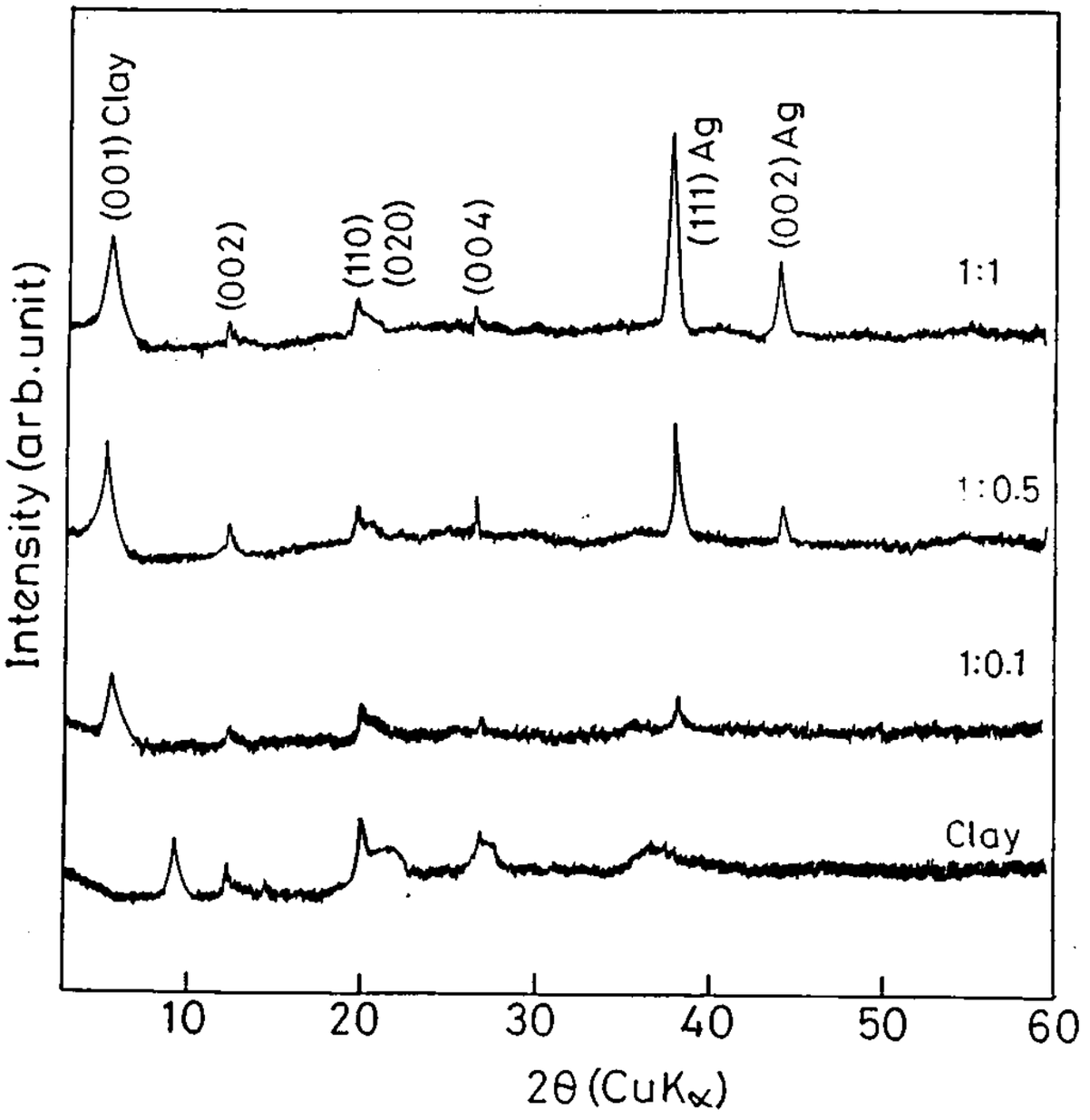

Fig. 6. X-ray diffraction patterns of the products obtained by ethylene glycol reduction of $AgNO_3$ intercalated montmorillonite. The (111) and (002) reflections of Ag metal can be seen.

reflections of the Ag metal appears. More importantly, the $I(001)_{clay}$ / $I(111)_{Ag}$ decreases with the increasing amount of silver in the starting composition. This is consistent with our expectation that greater amount of silver nitrate will intercalated in the composition containing higher proportions of the salt.

The TEM of the reduced samples and the extensively washed samples were taken and their average particle size determined (see Fig.7). The line width of the Ag peak becomes broader with the decrease in Ag content which means that the particle size decreases with the Ag content in the starting composition. We also find that the particle size decreases on washing (from 35 nm for the reduced sample to 20 nm for further washed sample). The d(001) changes from 9.83 Å in the starting material to 14.9 Å in the reduced sample indicating the presence of 5 Å clusters of silver in the inter layer of clay. We note that in addition to the intercalation of Ag metal inside the clay, a considerable amount of silver particles are present on the external surface of the clay. This explains the decrease in particle size on

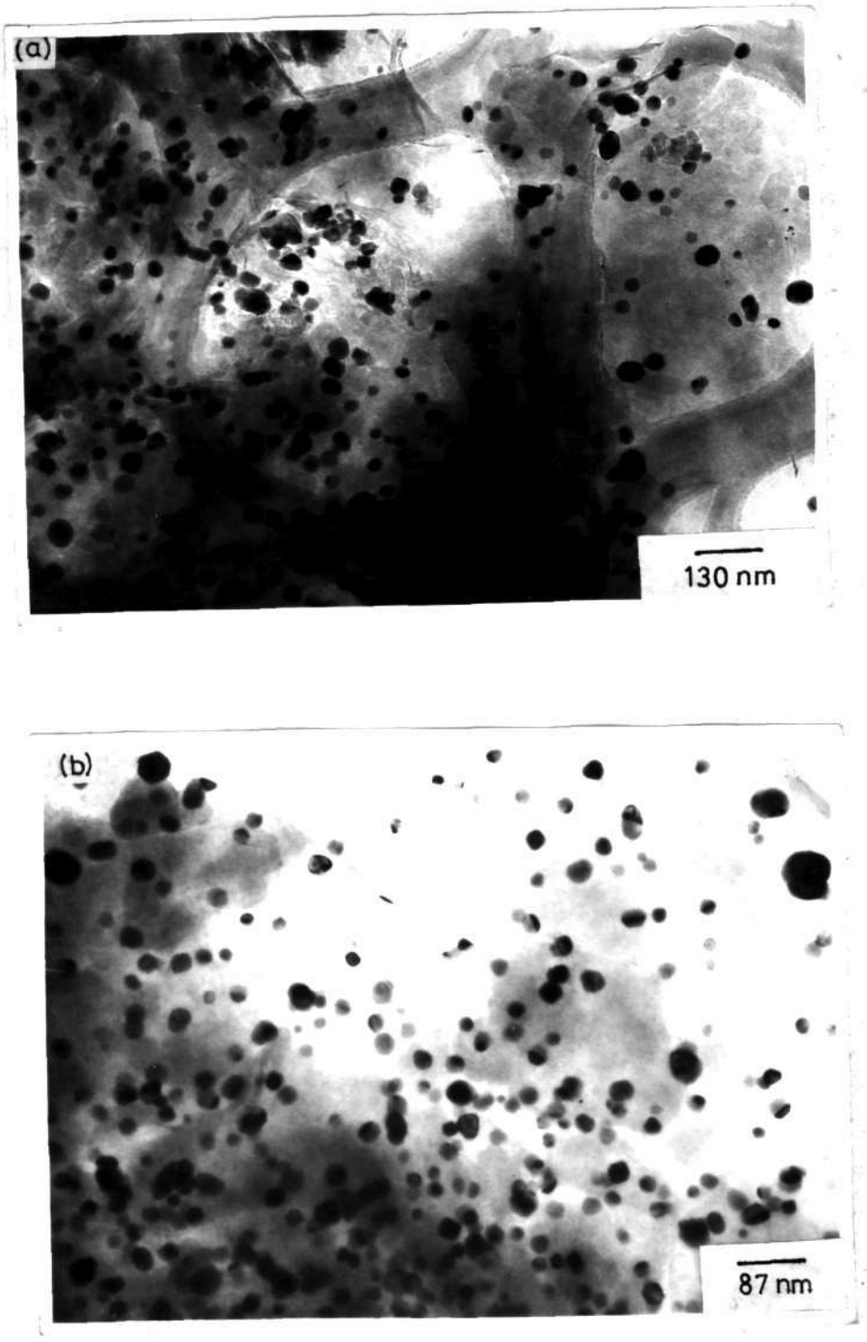

Fig. 7. Transmission electron micrographs showing Ag particles (a) obtained by ethylene glycol reduction of $AgNO_3$-clay intercalate (1:1 weight ratio) and (b) after extensive washing of (a).

washing. In Table 1 we have summarised all the properties of silver-intercalated clay samples.

Most of the nanoparticles of silver are probably produced by the reduction of the Ag salt that deintercalates from the clay leaving only the smallest metal clusters in between the layers of the clay. What is significant is that all the particles including those present outside the clay are in the nanometric regime.

Table 1 Properties of Ag/montmorillonite

Starting composition	d(001) of clay (Å)		I(001) clay[a] / I(111) Ag	Average particle diameter(nm)	
	after exchange	after reduction and washing		XRD[b]	TEM[c]
1:0.1	14.979	14.853	1.13	25	--
1:0.5	14.979	14.853	0.71	26	30
1:1	14.730	14.853	0.55	33	35

(a) After extensive washing, ratios were slightly higher in the 1:0.5 and 1:0.1 samples.

(b) The particle diameter remained the same even after extensive washing.

(c) After extensive washing, the diameter of 1:1 and 1:3 were around 20 and 30nm respectively.

Conclusions

In conclusion, we have been able to successfully prepare nanoparticles of Ag and Au. In the case of Cu, the nanoparticles were not as good although the particles obtained are in the right size range. Where ethanol alone fails, addition of magnesium reduces the metal the metal salt. It was necessary to use appropriate amount of PVP inorder to obtain a narrow size distribution of the metal particles.

In the case of silver-montmorillonite, we have been able to obtain nanoparticles of the metal by the reduction of silver intercalate by ethylene glycol. Apart from the silver metal particles formed by the reduction of the salt coming out of the interlayers, Ag clusters of 5 Å are present inside the interlayers as revealed by the d(001) value.

References

1. C. N. R. Rao, *Chemical approaches to the synthesis of inorganic materials*, John Wiley, Chichester (1994).
2. C. Ducamp-Sanguesa, R. Herrara-Urbina, M. Figlarz, *J. Solid State Chem.*, **100**, 272 (1992).
3. F. Fievet, J. P. Lagier, M. Figlarz, *MRS Bull.*, **29** (1989).
4. H. N. Vasan, C. N. R. Rao, *J. Mater. Chem.*, **5**, 1755 (1995).
5. P. B. Malla, P. Ravindranathan, S. Komarneni, R. Roy, *Nature*, **351**, 555 (1991).
6. P. R. Van Rheenen, M. J. McKelvy, W. S. Glaunsinger, *J. Solid State Chem.*, **67**, 151 (1987).
7. S. Puvadda, S. Baral, G. M. Chow, S. B. Quadri, B. R. Ratna, *J. Am.Chem. Soc.*, **116**, 2135 (1994).
8. R. E. Grim, *Clay Mineralogy* (McGraw- Hill, NewYork), 1968.
9. P. P. Alphonse, M. Brieu, M. Gillet, P. Mauret, *J. Chim. Physique*, **85**, 6 (1988).
10. H. Torigoe, K. Esumi, *Langmuir*, **9**, 1664 (1993).